

Concentrating solar thermoelectric generators with a peak efficiency of 7.4%

Daniel Kraemer,¹ Qing Jie,² Kenneth McEnaney,¹ Feng Cao,² Weishu Liu,² Lee A. Weinstein,¹ James Loomis,¹ Zhifeng Ren,^{2*} and Gang Chen^{1*}

¹*Department of Mechanical Engineering, Massachusetts Institute of Technology, Cambridge, Massachusetts 02139, USA*

²*Department of Physics and TcSUH, University of Houston, Houston, Texas 77204, USA*

Concentrating solar power normally employs mechanical heat engines and is thus only used in large-scale power plants; however, it is compatible with inexpensive thermal storage enabling electricity dispatchability. Concentrating solar thermoelectric generators (STEGs) have the advantage of replacing the mechanical power block with a solid-state heat engine based on the Seebeck effect, simplifying the system. The highest reported efficiency of STEGs so far is 5.2%. Here, we report experimental measurements of STEGs with a peak efficiency of 9.6% at an optically concentrated normal solar irradiance of 211 kW m⁻², and a system efficiency of 7.4% after considering optical concentration losses. The performance improvement is achieved by the use of segmented thermoelectric legs, a high-temperature spectrally-selective solar absorber enabling stable vacuum operation with absorber temperatures up to 600°C, and combining optical and thermal concentration. Our work suggests that concentrating STEGs have the potential to become a promising alternative solar energy technology.

* Corresponding authors, gchen2@mit.edu, zren@uh.edu

At present, the two main methods of converting sunlight into electricity are solar photovoltaic, which is based on electron and hole generation in semiconductors; and concentrating solar power (CSP), which constitutes converting light into heat to drive mechanical heat engines.¹⁻⁶ The conversion of solar energy into electricity via solid-state thermoelectric generators has a long history,^{7,8} with the best efficiency reported by some of us at 5.2% using 1.5 optical concentration of sunlight in combination with thermal concentration of solar energy by heat conduction.⁹ Modeling shows that further increase in efficiency is possible with higher optical concentration for devices to operate at higher temperatures.^{10,11} Inspired by the modeling and continued progress in thermoelectric materials research,¹²⁻²² we construct and test concentrated solar thermoelectric generators (CSTEG) and report here experimentally measured STEG and CSTEG efficiencies peaking at 9.6% and 7.4%, respectively. Here, the STEG efficiency is based on the concentrated direct normal irradiance on the solar absorber for consistent comparison with previous reports; and CSTEG efficiency includes optical concentration losses of our experimental system and 90% of direct sunlight of one sun corresponding to 1 kW m^{-2} . The record-high efficiencies are achieved by segmenting two thermoelectric materials, skutterudite and bismuth telluride, coupled to a spectrally selective surface operated at close to 600°C by combined optical and thermal concentration of the sunlight.

CSTEG Efficiency. We use a simplified model here to guide the discussion, although the actual modeling results presented in the manuscript are based on a model that includes parasitic losses in great detail and can be found in previous publications and in Supplementary Method S1.^{9,11,23} The efficiency (η) of a CSTEG can be approximately expressed as the product of the

optical efficiency (η_{opt}), the absorber efficiency (η_{abs}), the TEG efficiency (η_{teg}) and the auxiliary efficiency (η_{aux})²³

$$\eta = \eta_{opt}\eta_{abs}\eta_{teg}\eta_{aux} \quad (1)$$

The optical efficiency is determined by optical losses from the concentrating optics (including the loss of the diffuse light portion), and possible glass transmission affecting the solar radiation flux incident on the solar absorber (q_{abs}). We define the geometric optical concentration, $C_{opt} = A_{ap}/A_{abs}$ as the area ratio between the aperture of the concentrating optics (A_{ap}) and the solar absorber (A_{abs}), and relate q_{abs} to the incident solar intensity q_{sol} via $q_{abs} = \eta_{opt}C_{opt}q_{sol}$. The absorber efficiency is the measure of how efficiently the sunlight incident on the solar absorber is converted into a heat flowing through the TEG. Under the assumption of a uniform absorber temperature the absorber efficiency can be estimated for a STEG in a vacuum environment with²³

$$\eta_{abs} = \alpha_{sol} - \frac{\varepsilon\sigma_{sb}(T_{abs}^4 - T_{amb}^4)}{\eta_{opt}C_{opt}q_{sol}} \quad (2)$$

With T_{amb} being the surrounding ambient temperature, σ_{sb} being the Stefan-Boltzmann constant, α_{sol} the solar absorptance and ε the emittance of the solar absorber at temperature T_{abs} . The efficiency of an ideal thermoelectric generator (η_{teg}) can be expressed as

$$\eta_{teg} = \frac{T_h - T_c}{T_h} \frac{\sqrt{1 + \overline{ZT}} - 1}{\sqrt{1 + \overline{ZT}} + \frac{T_c}{T_h}} \quad (3)$$

where T_c is the cold-side temperature, T_h the hot-side temperature, and \overline{ZT} the effective figure of merit of the thermoelectric materials when operated between T_c and T_h .^{24,25} Additional device specific parasitic losses such as the materials' compatibility, electrical contact and wire resistances and radiation heat transfer losses from the thermoelectric couple generator affect the

device performance. The effective figure of merit can be calculated from Eq. (3) together with either the experimentally obtained or simulated (see Supplementary Methods S1 and S3) TEG efficiency. The effective figure of merit will be lower than the thermoelectric materials' figure of merit (ZT) (averaged over the operating temperature different) defined as $ZT = (S^2\sigma/k)T$, where S , σ , k , and T are the Seebeck coefficient, electrical conductivity, thermal conductivity, and absolute temperature, respectively.^{26,27} Significant progress has been made on improving and developing new thermoelectric materials in recent years, however actual device demonstrations have been scarce and are mostly motivated by waste heat recovery applications.^{28–34}

The auxiliary efficiency in Eq. (1) accounts for possible system parasitic losses such as electricity consumption for pumping and cooling. This efficiency can be close to one for a STEG design that does not involve a high-temperature working fluid and can rely on heat spreading and passive cooling. Our past work suggests heat spreading up to several thousand times will not incur much temperature drop due to the small cross-sectional area of the thermoelectric legs,⁹ which suggests passive cooling by natural convection is possible. Thus, we assume a 100% auxiliary efficiency in the rest of this paper. In our actual experiment, due to the constraints of the vacuum chamber environment, we manage the cold side heat load using an actively cooled heat sink, which also serves to maintain a constant temperature.

Previous STEG and CSTEg Demonstrations. We previously reported a STEG with an efficiency of 4.6% under one sun condition (1 kW m^{-2}) without optical concentration ($C_{\text{opt}} = 1$ in Eq. (2)).⁹ For that demonstration, our STEG design concentrated the absorbed solar energy to the thermoelectric elements via heat conduction. The required geometric thermal concentration ratio, defined as the ratio of the solar absorber area to the cross-sectional area of the thermoelectric legs, was around 300. In this case, the optimal operating temperature of the solar

absorber was approximately 200°C. This relatively low optimal operating temperature is determined by the competition of increasing η_{teg} and decreasing η_{abs} with rising absorber temperature as seen from Eqs. (2) and (3). By using optical concentration, η_{abs} can be increased according to Eq. (2) and the optimal operational temperature shifts to higher temperatures. We achieved a STEG efficiency of 5.2% at a solar irradiance of 1.5 kW m⁻². Preceding efforts on terrestrial CSTEGBs were limited to significantly lower efficiencies.^{7,35–38} One of the highest STEG efficiencies of 3.35% was demonstrated in 1954 with a geometric optical concentration ratio of 50, and for many decades subsequent experimental efforts did not lead to better results.⁷ A CSTEGB based on bismuth telluride materials with a stationary concentrator achieved an efficiency of ~1% (excluding optical losses) in 1980 at an estimated optical concentration of 2.7X.³⁵ In 1982 a CSTEGB prototype was developed for high solar concentration using a solar furnace and lead telluride material permitting larger temperature differences.³⁶ However, the reported STEG efficiencies were 30% higher than their predicted maximum TEG efficiency of only 4% raising significant doubts in the experiments. In 1998 an efficiency of ~0.9% was demonstrated with a conceptual CSTEGB experiment using a commercial bismuth telluride based module and an infrared heat lamp providing an absorber solar irradiance of 20 kW m⁻².³⁷ In 2010 efforts were made to develop a cost-competitive CSTEGB design for micropower applications in developing countries using a commercial bismuth telluride based module and a low-cost concentrator.³⁸ A STEG efficiency of 3% (excluding optical losses) was demonstrated at an absorber solar irradiance of 66 kW m⁻².

The low STEG efficiencies experimentally achieved in the past with CSTEGBs is mainly due to one or more of the following factors: (1) the lack of good thermoelectric materials working over a large temperature range, (2) the lack of high-temperature spectrally selective surfaces

minimizing the emittance ϵ in Eq. (2), and (3) the mismatch between the thermoelectric modules and the solar absorbers. Thermoelectric materials typically perform best in a relatively narrow temperature range.^{11,27,31,33,39} Modeling has shown that higher performance can be achieved by segmenting thermoelectric legs with different materials permitting large operating temperature differences.^{11,39} For example, by using a low-temperature material such as bismuth telluride operating up to ~ 250 °C and a high-temperature material such as skutterudite operating above ~ 250 °C, a CSTEg can theoretically achieve an efficiency of over 10%.¹¹ In this paper, we experimentally demonstrate a maximum STEg efficiency of 9.6% at a concentrated direct normal solar irradiance (DNI) of 211 kW m^{-2} (excluding optical losses). The demonstrated CSTEg efficiency is 7.4% which includes the optical losses from the used glass viewport and focusing lens (Supplementary Fig. 9c) and an assumed diffuse light fraction loss of 10% (DNI of 0.9 kW m^{-2}) resulting in an experiment-specific optical efficiency of ~ 0.77 . Our experimental results are in reasonable agreement with theoretical predictions.

CSTEg Design and Fabrication. The record-high STEg and CSTEg efficiencies are achieved by using TEGs based on a pair of n/p-type segmented thermoelectric legs consisting of doped bismuth telluride and skutterudite materials enabling hot-side temperatures up to 600°C while the cold side was maintained at 25°C (Fig.1). Device design, modeling, fabrication details, and materials properties are given in the Methods Section, Supplementary Table 1 and Supplementary Method S2. The STEGs are operated under vacuum to eliminate air convection and conduction losses and to ensure high-temperature stability. The use of a recently developed high-temperature stable spectrally-selective solar absorber further reduces infrared radiation heat losses without significantly affecting the absorption of the sunlight (Supplementary Fig. 5).^{40,41}

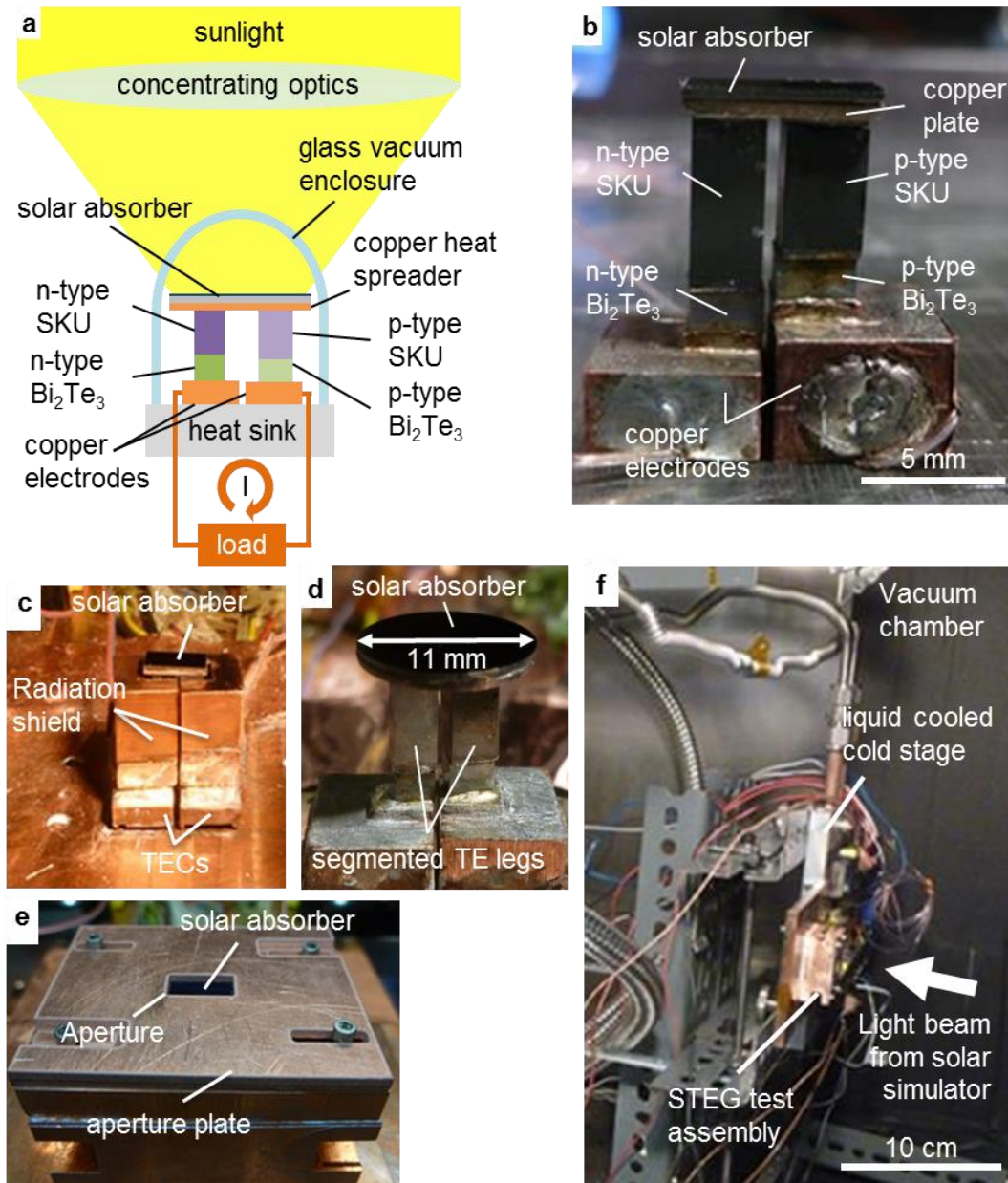


Figure 1 | CSTEG concept and proof-of-concept experiment. (a) Illustration of a CSTEG based on a pair of segmented p/n-type thermoelectric (TE) legs consisting of doped bismuth telluride (Bi_2Te_3) and skutterudite (SKU) materials. The segmented legs are sandwiched between a high-temperature spectrally-selective solar absorber and a heat sink with copper electrodes and surrounded by a glass vacuum enclosure. Concentrating optics focuses the incident sunlight onto the solar absorber. (b) STEG cell optimized for high optical concentration ($\sim 200\times$) with geometric thermal concentration ratio, C_{th} , of 1.4. (c) STEG cell with TE leg radiation shields soldered onto thermoelectric coolers (TECs) (d) STEG cell optimized for moderate optical concentration ($\sim 50\times$) with $C_{\text{th}} = 5.4$. (e) STEG test assembly with thermally grounded aperture plate. (f) STEG test setup with liquid cooled cold stage inside vacuum chamber.

Two devices were fabricated, one using high optical solar concentration to minimize the effect of thermal heat losses which requires 2-axis tracking, and the other at moderate optical concentration to be compatible with 1-axis tracking.⁴ Both devices combine optical and thermal concentration. The geometric thermal concentration ratio, C_{th} is defined as the ratio of the absorber area to the TEG cross-sectional area (A_{abs}/A_{teg}).⁹ At high optical solar concentration ($C_{opt} \approx 200$) a C_{th} of 1.4 is required for a combined concentration ratio (CCR) of ~ 280 to match the hot-junction heat flux of the TEG, leading to a typical solar absorber area of $\sim 24.5 \text{ mm}^2$ (Fig. 1b and c). The STEG optimized for moderate optical solar concentration ($C_{opt} \approx 50$) uses C_{th} of 5.4, corresponding to a solar absorber area of $\sim 95 \text{ mm}^2$ (Fig. 1d) and CCR of ~ 270 . Both STEGs are fabricated with a solar absorber based on a spectrally-selective double cermet multilayer stack.⁴¹ The STEG for high optical concentration is also fabricated with a reference black paint (HE6) as solar absorber surface (Supplementary Fig. 7).^{40,42}

CSTEG Performance. Figures 2a and b show the performance of our fabricated STEGs with spectrally-selective (ss) and black paint (bp) solar absorbers as a function of thermoelectric current at solar irradiances of 211 kW m^{-2} and 215 kW m^{-2} , respectively, for the device with high optical solar concentration ($C_{opt} \approx 200$, $C_{th} = 1.4$, $CCR \approx 280$). The STEG with the spectrally-selective solar absorber peaks at a record-high efficiency of 9.6%, which is almost 3 times more efficient than Telkes' best device and twice as efficient as our previous work (Fig. 2a).^{7,9} As expected from Eq. (2), at high solar irradiances the STEG with the black paint solar absorber performs with a similar peak efficiency of 8.9% because the high optical concentration effectively reduces radiation heat loss. The STEG power output reaches 0.5 W (Fig. 2b) corresponding to a power output density of $\sim 30 \text{ kW m}^{-2}$ based on the cross-sectional area of the single couple TEG. At each solar irradiance set point the I-V curve measurement itself takes up

to two hours depending on the number of current set points to allow the STEG to reach its steady state at each current setting. No significant degradation of the STEG was observed in that time frame which is supported by the expected linear behavior of the I-V curves.

The STEG performances peak at solar irradiances of approximately 200 to 225 kW m⁻² and the STEGs operate with an absorber temperature of approximately 560 to 580 °C (Fig. 2c and d) [see Methods for determination of absorber temperature]. For a decrease in the solar flux density by a factor of two we observe a drop in the STEG efficiency of approximately 17% which is smaller compared to what was previously observed for a purely thermally-concentrating STEG with a drop of approximately 25%.⁹ The operating temperature of the solar absorber correspondingly falls to approximately 350 °C (Fig. 2d). The solar intensity varies over the course of a day. However, the tracking of the sun required for the concentrating optics leads to a reduction of this intensity variation.⁴ Nevertheless, CSTEGBs with optical solar concentration should be optimized for maximum yearly energy output depending on its location and the level of optical concentration used.^{9,23} Concentrating optics cannot focus diffuse light, thus, CSTEGBs perform best in locations with high DNI.

We further determined the TEG efficiency (η_{teg}) as a function of the solar irradiance close to 11% for the segmented TEG operating between 25 °C and approximately 570 °C (Fig. 2e) [see Methods Section]. This device efficiency corresponds to an effective ZT of ~0.64 which is significantly lower than the average material ZT of ~1.02 due to contact resistances, the infrared radiation losses from the thermoelectric legs and the radiative thermal shunting losses from the hot side to the cold side. Additionally, the uncertainties in the thermoelectric material properties might also contribute to the discrepancy in ZT. As expected, the determined absorber efficiency of approximately 90% for the spectrally-selective solar absorber (Fig. 2f) is higher than that for

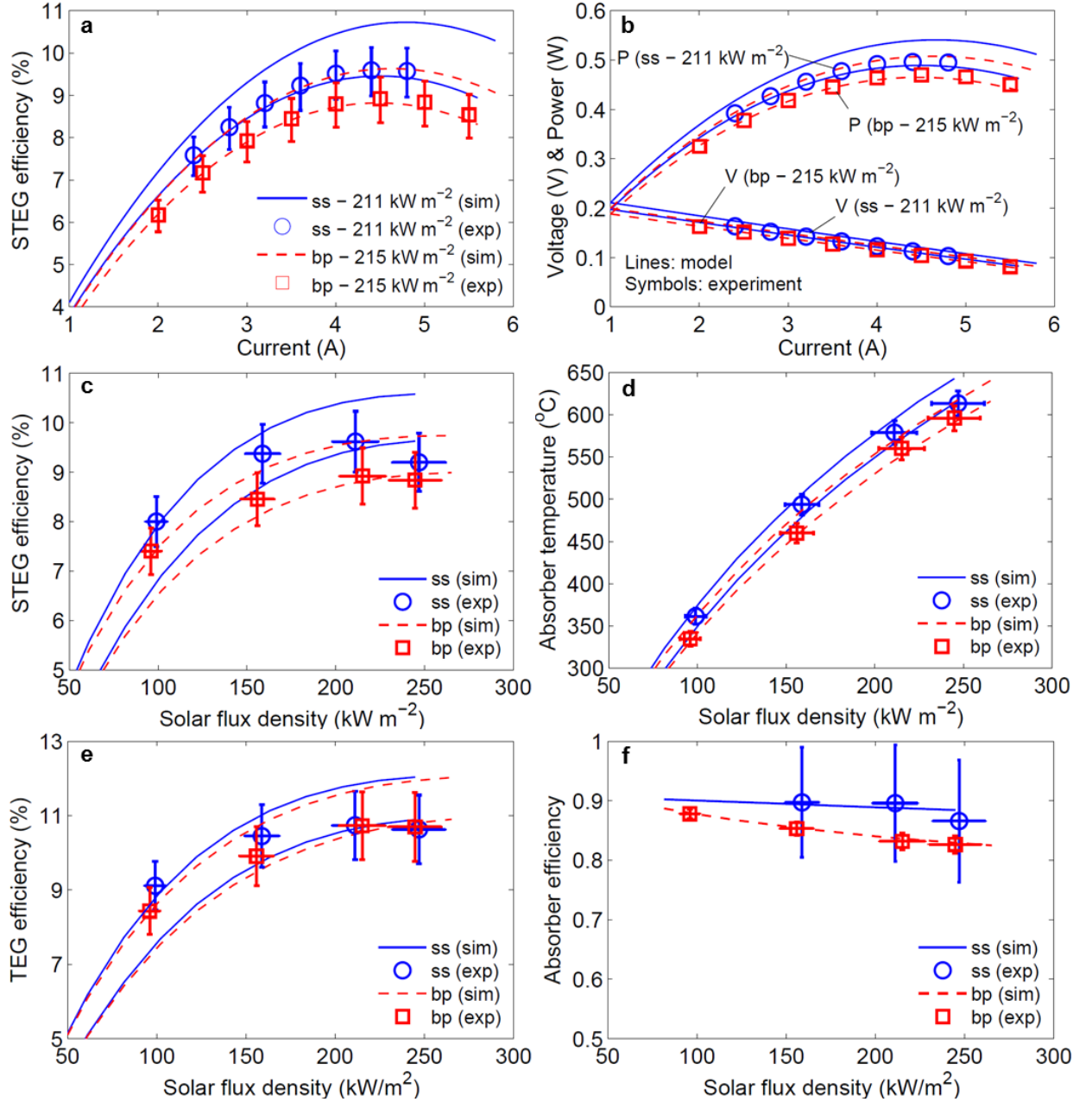


Figure 2 | Performance characteristics of a STEG optimized for high optical concentration.

Typical STEG performance characteristics at high solar flux densities and small thermal concentration ratio (C_{th}) of 1.4 with high-temperature spectrally-selective (ss) and black paint (bp) solar absorbers. Open squares and circles are experimental data, lines are modeling results of upper and lower bounds. (a) STEG efficiency versus electrical current of a STEG with ss at 211 kW m⁻² and bp at 215 kW m⁻² (b) I-V and I-P characteristics of a STEG with ss at 211 kW m⁻² and bp at 215 kW m⁻² (c) STEG efficiency, (d) absorber temperature, (e) TEG efficiency and (f) absorber efficiency as a function of incident solar flux density. Error bars in all subfigures are the result of uncertainty in incident radiation power measurement.

the black paint solar absorber. The discrepancy between experiment and modeling is larger at higher solar irradiances because the rising absorber temperature due to the fixed STEG geometry results in a disproportional increase of the infrared radiation heat loss which is more pronounced for the black paint compared to the low-emittance selective solar absorber. Another possible explanation is absorber damage since at $\sim 250 \text{ kW m}^{-2}$, the absorber operating temperature is above 600°C (Fig.2d) while the double-cermet absorber was only proven to be stable in vacuum up to 600°C .⁴¹ Overall, however, the gain in efficiency by using a spectrally-selective solar absorber instead of black paint at such high optical solar concentration is not substantial and might not justify the increased complexity in the STEG fabrication.

Figure 3 shows the results of a STEG optimized for moderate optical concentration ($C_{\text{opt}} \approx 50$, $C_{\text{th}} = 5.4$, $\text{CCR} \approx 270$). The larger thermal radiation heat loss of the solar absorber limits the peak STEG efficiency to 7.6% and the peak power output to close to 0.3 W at a solar irradiance of $\sim 38 \text{ kW m}^{-2}$ (Fig. 3a and b). The absorber operating temperature at peak STEG performance is approximately 420°C . Even though the performance is worse compared to STEGs optimized for high optical solar concentration, it is still a remarkable improvement over previous reports in the literature (Fig. 3c).^{7,9,10,35,37,38,43,44} All reported STEG efficiencies in Fig.3c are based on the solar radiation power incident on the solar absorber, thus, excluding the optical losses from concentrating optics. The record-high STEG efficiencies demonstrated here at moderate and high solar irradiances of $\sim 38 \text{ kW m}^{-2}$ and $\sim 210 \text{ kW m}^{-2}$ are still $\sim 2\text{--}3$ times higher compared to previously-reported best values for CSTEGBs with similar optical solar concentrations.^{7,38}

System Efficiency and Directions for Improvement. Our CSTEGB experiments are performed inside a vacuum chamber with a fused silica viewport (solar transmittance of ~ 0.93)

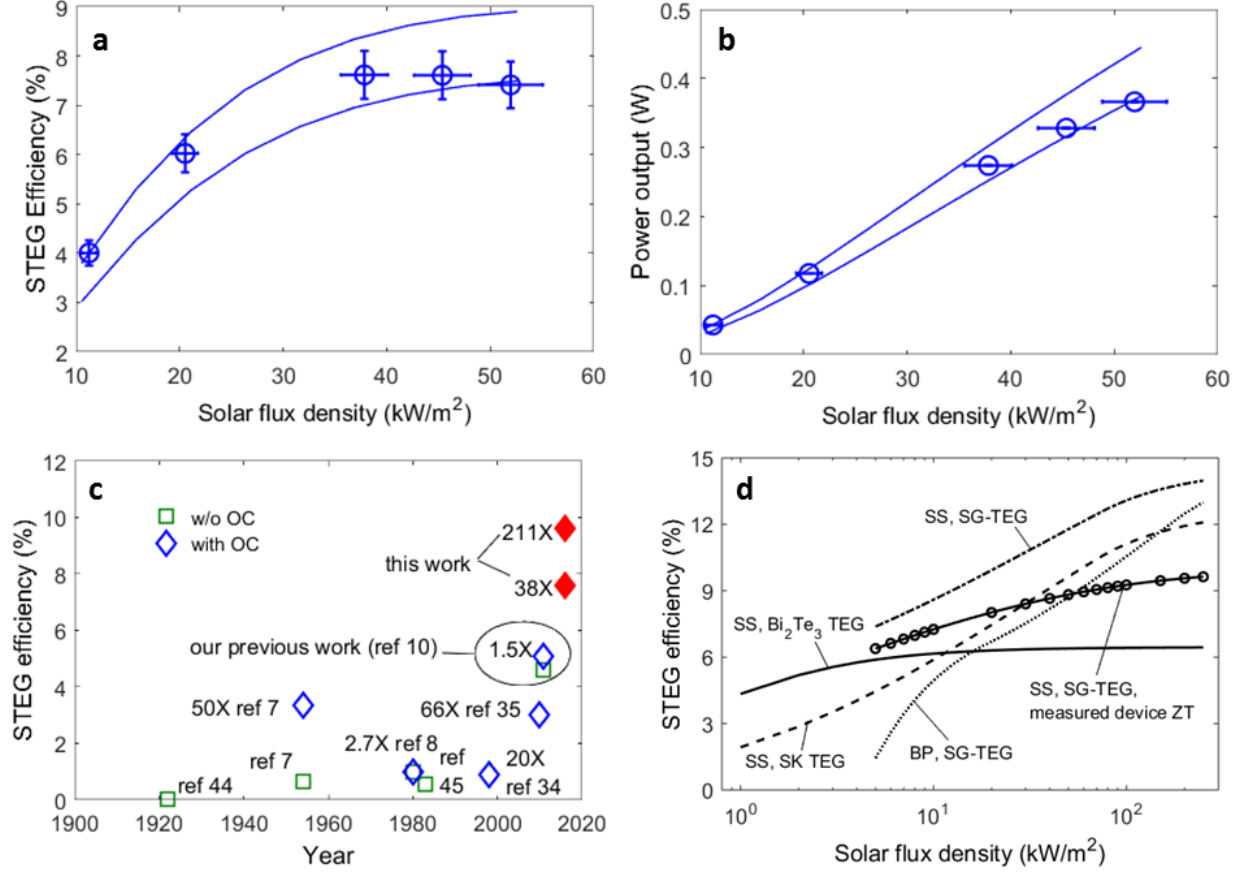


Figure 3 | Performance characteristics of a STEG optimized for moderate optical concentration. Typical STEG performance characteristics at moderate solar flux densities and thermal concentration ratio ($C_{\text{opt}} \approx 50$, $C_{\text{th}} = 5.4$, $\text{CCR} \approx 270$) with a high-temperature spectrally-selective solar absorber. Open circles are experimental data, lines are modeling results of upper and lower bounds. **(a)** STEG efficiency (at peak efficiency under 38 kW/m² illumination, absorber temperature is 420 °C) and **(b)** STEG output power. Error bars are the result of uncertainty in incident radiation power measurement. **(c)** Historical overview of experimental efficiency demonstrations of STEGs with (diamond symbol) and without (square symbol) optical concentration (OC). STEG efficiencies are based on the solar radiation flux incident on the solar absorber excluding optical losses from concentrating optics. **(d)** Simulated maximum efficiencies of STEGs with various design configurations optimized over a range of solar flux densities: STEG with spectrally-selective (SS) solar absorber and a TEG based on bismuth telluride (Bi_2Te_3) (solid line), skutterudite (SK, dashed line), segmented (SG, Bi_2Te_3 +skutterudite) legs (dash-dotted line) and a TEG based on our measured effective device ZT (solid line with open circles); STEG with back paint (BP) absorber and segmented TEG (dotted line).

and the solar radiation from the solar simulator is focused with an uncoated N-BK lens (solar transmittance of ~ 0.92) onto the STEG test assembly (Supplementary Fig. 9). Taking into account these optical losses and assuming a diffuse light fraction of 10% the highest demonstrated CSTEg efficiencies are $\sim 7.4\%$ and $\sim 5.9\%$ at high and moderate optical solar concentration, respectively. The performance improvements of our STEGs compared to previous works can mainly be attributed to the use of segmented thermoelectric legs consisting of low-temperature bismuth telluride and high-temperature skutterudite materials, a high-temperature spectrally-selective solar absorber and a vacuum environment (Fig. 3d). These three key design features enable a stable and efficient STEG operation with much larger operating temperature differences. The vacuum environment is essential not only for reducing heat losses but also for the high-temperature stability of the fabricated STEGs. The thermoelectric materials and the spectrally-selective solar absorber oxidize in air at high temperatures, detrimentally affecting their properties and the STEG performance.

Figure 3d illustrates theoretical calculations of various STEG configurations under vacuum for a range of incident solar flux densities. The calculations use the typical properties of the developed spectrally-selective solar absorber, bismuth telluride and skutterudite materials (Supplementary Fig. 1). The calculations do not take into account radiation losses from the thermoelectric legs and assume negligible contact resistances. Similar to most experimental efforts reported in literature, a STEG based on a low-temperature material such as bismuth telluride (Bi_2Te_3) is significantly limited in its efficiency due to the material's maximum operating temperature of $\sim 250^\circ\text{C}$ (Fig. 3d: solid line). High-temperature thermoelectric materials such as skutterudite enable operation with much larger temperature differences (Fig. 3d: dashed line). This can significantly increase the maximum achievable STEG

efficiency, despite the poor TEG performance at low temperatures. A STEG with segmented thermoelectric legs consisting of bismuth telluride as the low-temperature and skutterudite as the high-temperature section can exploit a large temperature difference more efficiently to further improve the STEG performance (Fig. 3d: dash-dotted line). The use of a spectrally-selective instead of a black paint solar absorber can boost the STEG efficiency especially of STEGs optimized for low and moderate optical solar concentrations (Fig. 3d: dash-dotted and dotted lines). Figure 3d also illustrates the simulated STEG performance using the effective device ZT (solid line with open circles) that is obtained from our demonstrated TEG efficiencies (Fig. 2e). This effective device ZT is substantially lower compared to the average materials ZT due to experimental imperfections such as electrical contact resistances and radiation heat losses. Thus, our lab scale device tests demonstrate a lower STEG performance than theoretically is achievable. This highlights the challenges and importance of thermoelectric device demonstrations in addition to materials development and properties measurements. Furthermore, the discrepancy between our experiments and the theoretical predictions of ~14% (Fig. 3d) suggests substantial room for further improvement in the efficiency of current STEGs by reducing the effects of electrical contact resistance and radiation heat losses. The negative impacts of contact resistance can be overcome by identifying better contacts or increasing the lengths of the thermoelectric legs; and radiation heat can be minimized by increasing the cross-sectional area to reduce relative radiation heat loss from side walls, or placing multiple legs close to each other.

The large CCR of up to 295X, achieved by combining optical and thermal concentration, enable our CSTEGBs to generate an electrical peak power output of up to ~0.5 W with only ~0.9 gram of thermoelectric material (Fig. 2b and 3b). At the current prices of the used bismuth

telluride and skutterudite based materials, the cost for the TEG's thermoelectric material is approximately \$26 per kg or \$0.046 per electrical peak watt generated (Supplementary Table 2). Although the device fabrication will certainly increase the cost beyond just materials cost, the low material cost is a good starting point. The amount of thermoelectric material can further be reduced without significantly affecting the STEG performance as long as the electrical contact resistance is small.²³ It should be acknowledged that our demonstrated peak TEG efficiency of about 11% is 3-4 times lower than the efficiencies of currently used mechanical heat engines.⁴⁵ Consequently, at the current state the demonstrated STEG is not yet competitive economically. However, TEGs with higher efficiencies have been reported.^{31,33} Additionally, there are several avenues to further improve the STEG performance: (1) increasing optical solar concentration which increases both η_{abs} and η_{teg} , (2) reducing the infrared emittance of the solar absorber, (3) improving thermoelectric materials, and (4) improving device design to minimize radiation losses from side walls of thermoelectric legs and from the back side and edges of the solar absorber. Figure 4a shows the predicted maximum efficiencies as a function of optical solar concentration for a STEG with an effective device ZT of 1 and based on a solar absorber with solar absorptance of 0.93 and several effective infrared emittance values. With a solar absorber temperature limited to 1000 °C a STEG can reach an efficiency of over 16% at optical solar concentration of 1000X. At such high optical concentration the infrared emittance of the solar absorber does not significantly affect the performance of the STEG despite the high operating temperature. Thus, the selective solar absorber can be replaced with a high-temperature stable black solar absorber/receiver which eliminates the challenge of developing a thermally stable selective solar absorber. Figure 4b shows the predicted maximum efficiencies as a function of optical solar concentration of a STEG based on a blackbody solar absorber for different effective

device ZTs. With an absorber temperature reaching close to 1000 °C and thermoelectric materials with an effective ZT of 2 the maximum STEG efficiency can reach close to 24%. However, operating a STEG with such a large operating temperature difference requires TEGs with thermoelectric materials that can operate efficiently at temperatures up to 1000 °C. Recent progress made in high-temperature thermoelectric materials and device demonstrations raises hope of achieving predicted efficiencies.^{19,31,33} One of the main advantages of CSP is dispatchability by using inexpensive thermal storage. Solar CSTEG can also be coupled to a

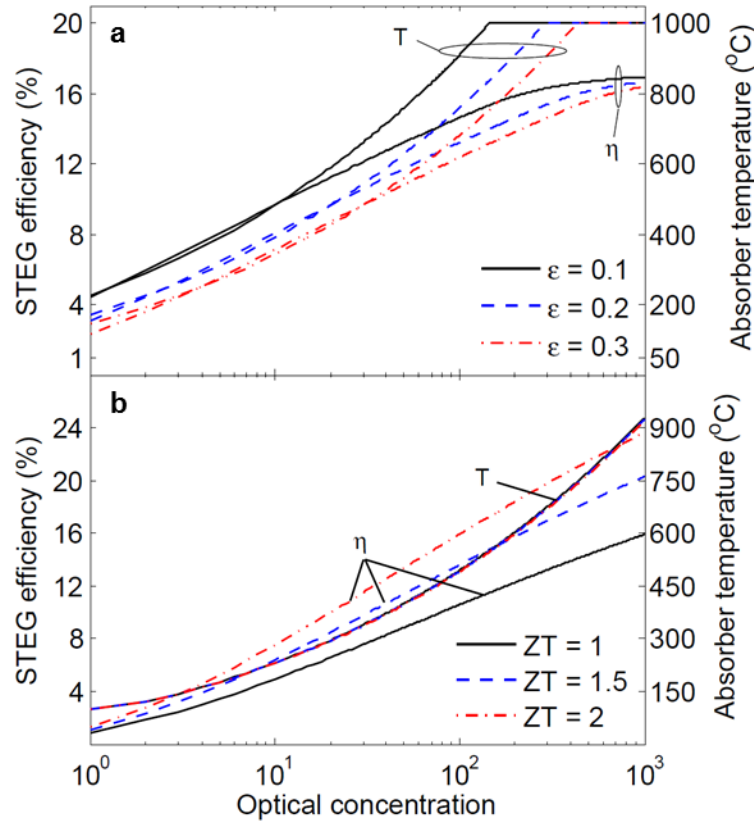


Figure 4 | Theoretical predictions of STEG efficiencies and corresponding optimal solar absorber temperatures. STEG efficiencies and optimal absorber temperatures are calculated as a function of optical concentration based on the solar radiation flux incident on the solar absorber. Solar absorber temperature is limited to 1000 °C and the cold-side temperature is 50 °C. (a) Simulated performance of a STEG with an effective ZT = 1 thermoelectric material and selective absorber with solar absorptance of 0.93 and IR emittance (ϵ) of 0.1, 0.2 and 0.3. (b)

STEG with a blackbody solar absorber (solar absorptance and IR emittance of 1) and thermoelectric material with effective ZT of 1, 1.5 and 2. thermal storage system, although the device and system configurations would need to be redesigned. Thus, future research should not only focus on improving the CSTEG efficiency but also on the incorporation of thermal storage. Our experimental results should stimulate such research.

Methods

Device Modeling and Optimization. The optimum design of CSTEGs depends on the incident solar radiation power, the solar absorber properties, the emittance values of surfaces participating in the CSTEG's radiative heat transfer with the surroundings, the thermoelectric material properties, the cold-side temperature, and the device geometry (Supplementary Fig. 2). The lengths of the bismuth telluride and skutterudite sections are optimized for highest segmented thermoelectric leg efficiency and the cross-sectional areas are optimized for highest TEG efficiency using a numerical solver based on the iterative method and the Domenicali's equations modified to include leg radiation losses, keeping in mind of the limits of the maximum current can be supplied by our instruments (Supplementary Method S1).^{11,23,46} For the given TEG geometry and with its calculated performance characteristics as a function of hot-junction temperature, the area of the solar absorber with known temperature-dependent properties is optimized to find the optimal thermal concentration for moderate and high incident solar radiation power densities.

The upper and lower bounds in Fig. 2 are calculated with the uncertainties in thermoelectric material properties and uncertainties in the optical properties of surfaces which participate in the radiation heat transfer affecting the STEG performance. We also take into account results from a TEG characterization experiment that shows the Seebeck voltage to be ~5% lower and the

electrical resistance to be ~12% higher than expected for our fabricated TEGs (Supplementary Method S3).

Device Fabrication. Details about the fabrication and properties of the used thermoelectric elements and solar absorbers as well as the fabrication and testing of the CSTEg assemblies are given in Supplementary Methods S2 and S3 and briefly summarized here. The individual thermoelectric elements (bismuth telluride and skutterudite) are fabricated with hot-pressed contact pads using a ball mill and a subsequent hot-press process (Supplementary Fig. 3).^{30,32,47} The segmented legs are fabricated by soldering the bismuth telluride and skutterudite elements to each other (Fig. 1b). The typical dimensions of the p-type segmented leg including contact pads is approximately $3 \times 3 \times 9 \text{ mm}^3$ with the bismuth telluride and skutterudite sections being 1.75 mm and 5.9 mm long, respectively. The n-type segmented leg is of similar dimensions. A copper plate is brazed to the skutterudite ends as the hot junction electrically connecting the n/p-type segmented legs in series. The solar absorber is fabricated on a stainless steel substrate which is brazed to the hot-junction copper plate. Here, the hot-junction plate helps minimize temperature gradients within the solar absorber. The cold-junction copper electrodes for each of two bismuth-telluride legs are soldered onto individual thermoelectric coolers which are attached to a liquid-cooled stage for accurate and stable temperature control during the CSTEg device tests (Supplementary Fig. 6a). The segmented thermoelectric legs consisting of bismuth telluride and skutterudite materials are surrounded by tight copper radiation shields to reduce radiation heat loss.

The used spectrally-selective solar absorber is based on a double-cermet layer (W/Ni-filled Al_2O_3) deposited on a stainless steel substrate and is thermally stable in vacuum up to 600 °C (Supplementary Fig. 4).⁴¹ The solar absorber has a temperature-independent solar absorptance of

approximately 0.91 and measured infrared total hemispherical emittance of ~ 0.15 at $500\text{ }^{\circ}\text{C}$ which can be extrapolated to ~ 0.18 at $600\text{ }^{\circ}\text{C}$. The high-temperature reference paint HE6 by Rolls Royce is applied on a stainless steel substrate and used as the black paint solar absorber with a temperature-independent solar absorptance and total-hemispherical emittance of 0.95 (Supplementary Fig. 6g).^{40,42}

Device Testing. The STEG assembly is mounted onto a liquid cooled cold stage to minimize thermal drift and tested inside a vacuum chamber with a fused silica viewport under concentrated solar radiation from a solar simulator (Fig. 1f). The vacuum levels during the CSTEg experiments are maintained between 1×10^{-3} and 1×10^{-2} Pa. The measurement of the incident solar radiation power, Q_{abs} , is performed before and after the CSTEg experiment using a calibrated thermopile and power meter from Newport (Supplementary Method S3). The incident solar radiation power striking the solar absorber is accurately defined by a thermally grounded aperture placed in front of the solar absorber (Figs. 1c and 1e, Supplementary Fig. 6). The aperture opening has the same dimensions as and is aligned with the solar absorber.

A precision power supply and digital multimeter from Keithley is used to perform the current-voltage (I-V) curve measurements at constant solar radiation power striking the solar absorber ($Q_{\text{abs}} = A_{\text{abs}}q_{\text{abs}}$). The current voltage (I-V) curves (Fig. 2b) show the typical linear (resistive) behavior of a TEG with constant temperature difference,²⁷ indicating that the decreasing absorber temperature due to the Peltier effect does not introduce a substantial nonlinearity in the I-V relation. From this data the peak STEG efficiency $\eta = IV/Q_{\text{abs}}$ can be found. This efficiency does not include the optical losses. The transmittance of the used viewport and focusing lens is measured separately to estimate the optical losses (Supplementary Fig. 8).

In order to minimize heat losses, the solar absorber temperature is not measured in situ during the CSTEG experiments. Instead the fabricated STEGs are characterized in terms of their voltage output and electrical resistance as a function of hot-junction temperature by conducting a TEG characterization experiment (Supplementary Fig. 10). Using that information the absorber operating temperatures during the CSTEG experiment is measured using the TEG itself. With the measured STEG efficiency, the absorber temperature and the optical properties of the reference black paint (HE6: $\alpha_{\text{sol}} = \varepsilon = 0.95$), the absorber and TEG efficiencies can be calculated as a function of solar radiation flux using Eq. (2) and Eq. (1), respectively (Figs.2e and 2f). More details are given in Supplementary Method S3.

References:

1. Jones-albertus, R., Feldman, D., Fu, R., Horowitz, K. & Woodhouse, M. *Technology Advances Needed for Photovoltaics to Achieve Widespread Grid Price Parity*. (2015).
2. Luque, A. & Hegedus, S. *Handbook of Photovoltaic Science and Engineering*. (John Wiley & Sons, Inc., 2003).
3. Green, M. A. *Third Generation Photovoltaics: Advanced Solar Energy Conversion*. (Springer, 2003).
4. John A. Duffie, W. A. B. *Solar Engineering of Thermal Processes*. (2013).
5. Mills, D. Advances in solar thermal electricity technology. *Sol. Energy* **76**, 19–31 (2004).
6. Weinstein, L. A. *et al.* Concentrating Solar Power. *Chem. Rev.* **115**, 12797–12838 (2015).
7. Telkes, M. Solar Thermoelectric Generators. *J. Appl. Phys.* **25**, 765–777 (1954).
8. Goldsmid, H. J. *Applications of Thermoelectricity*. (Methuen, 1960).
9. Kraemer, D. *et al.* High-performance flat-panel solar thermoelectric generators with high thermal concentration. *Nat. Mater.* **10**, 532–8 (2011).
10. McEnaney, K., Kraemer, D. & Chen, G. Direct Heat-to-Electricity Conversion of Solar Energy. *Annu. Rev. Heat Transf.* 179–230 (2012). doi:10.1615/AnnualRevHeatTransfer.2012004544
11. McEnaney, K., Kraemer, D., Ren, Z. & Chen, G. Modeling of concentrating solar thermoelectric generators. *J. Appl. Phys.* **110**, 074502–8 (2011).
12. Venkatasubramanian, R., Siivola, E., Colpitts, T. & O’Quinn, B. Thin-film thermoelectric devices with high room-temperature figures of merit. *Nature* **413**, 597–602 (2001).

13. Harman, T. C., Taylor, P. J., Walsh, M. P. & Laforge, B. E. Quantum Dot Superlattice Thermoelectric Materials and Devices. *Science* **297**, 2229–2232 (2002).
14. Dresselhaus, M. S. *et al.* New Directions for Low-Dimensional Thermoelectric Materials. *Adv. Mater.* **19**, 1043–1053 (2007).
15. Poudel, B. *et al.* High-thermoelectric performance of nanostructured bismuth antimony telluride bulk alloys. *Science* (80-.). **320**, 634–638 (2008).
16. Heremans, J. P. *et al.* Enhancement of Thermoelectric Efficiency in PbTe by Distortion of the Electronic Density of States. *Science* **321**, 1457–1461 (2008).
17. Snyder, G. J. & Toberer, E. S. Complex thermoelectric materials. *Nat. Mater.* **7**, 105–14 (2008).
18. Biswas, K. *et al.* High-performance bulk thermoelectrics with all-scale hierarchical architectures. *Nature* **489**, 414–8 (2012).
19. Zhao, L.-D. *et al.* Ultralow thermal conductivity and high thermoelectric figure of merit in SnSe crystals. *Nature* **508**, 373–377 (2014).
20. Kim, S. I. *et al.* Dense dislocation arrays embedded in grain boundaries for high-performance bulk thermoelectrics. *Science* **348**, 109–114 (2015).
21. Beekman, M., Morelli, D. T. & Nolas, G. S. Better thermoelectrics through glass-like crystals. *Nat. Mater.* **14**, 1182–1185 (2015).
22. Zhao, L. *et al.* Ultrahigh power factor and thermoelectric performance in hole-doped single-crystal SnSe. *Science* (2015). doi:10.1126/science.aad3749
23. Kraemer, D., McEnaney, K., Chiesa, M. & Chen, G. Modeling and optimization of solar thermoelectric generators for terrestrial applications. *Sol. Energy* **86**, 1338–1350 (2012).
24. Kim, H. S., Liu, W., Chen, G., Chu, C.-W. & Ren, Z. Relationship between thermoelectric figure of merit and energy conversion efficiency. *Proc. Natl. Acad. Sci. U. S. A.* **112**, 8205–10 (2015).
25. Snyder, G. J. Application of the compatibility factor to the design of segmented and cascaded thermoelectric generators. *Appl. Phys. Lett.* **84**, 2436 (2004).
26. Ioffe, A. F. *Semiconductor Thermoelements and thermo-electric cooling*. (Infosearch Ltd, 1957).
27. Rowe, D. M. *Thermoelectrics Handbook: Macro to Nano*. (Taylor & Francis Group, LLC, 2006).
28. El-Genk, M. S., Saber, H. H., Sakamoto, J. & Caillat, T. Life Tests of a Skutterudites Thermoelectric Unicouple (MAR-03). in *22nd International Conference on Thermoelectrics* 417–420 (2003).
29. Guo, J. Q. *et al.* Development of Skutterudite Thermoelectric Materials and Modules. *J. Electron. Mater.* **41**, 1036–1042 (2012).
30. Muto, A., Yang, J., Poudel, B., Ren, Z. & Chen, G. Skutterudite Unicouple Characterization for Energy Harvesting Applications. *Adv. Energy Mater.* **3**, 245–251 (2013).
31. Caillat, T. *et al.* Progress Status of the Development of High-Efficiency Segmented

- Thermoelectric Couples. *Nucl. Emerg. Technol. Sp.* (2012).
32. Kraemer, D. *et al.* High thermoelectric conversion efficiency of MgAgSb-based material with hot-pressed contacts. *Energy Environ. Sci.* **8**, 1299–1308 (2015).
 33. Cook, B. A. *et al.* High-Performance Three-Stage Cascade Thermoelectric Devices with 20% Efficiency. *J. Electron. Mater.* **44**, 1936–1942 (2015).
 34. Salvador, J. R. *et al.* Conversion efficiency of skutterudite-based thermoelectric modules. *Phys. Chem. Chem. Phys.* **16**, 12510–20 (2014).
 35. Goldsmid, H. J., Giutronich, J. E. & Kaila, M. M. Solar thermoelectric generation using bismuth telluride alloys. *Sol. Energy* **24**, 435–440 (1980).
 36. Dent, C. L. & Cobble, M. H. A solar thermoelectric generator experiments and analysis. in *4th International Conference on Thermoelectric Energy Conversion* 75–78 (1982).
 37. Omer, S. Design optimization of thermoelectric devices for solar power generation. *Sol. Energy Mater. Sol. Cells* **53**, 67–82 (1998).
 38. Amatya, R. & Ram, R. J. Solar Thermoelectric Generator for Micropower Applications. *J. Electron. Mater.* **39**, 1735–1740 (2010).
 39. Baranowski, L. L., Snyder, G. J. & Toberer, E. S. Concentrated solar thermoelectric generators. *Energy Environ. Sci.* **5**, 9055–9067 (2012).
 40. Kraemer, D., McEnaney, K., Cao, F., Ren, Z. & Chen, G. Accurate determination of the total hemispherical emittance and solar absorptance of opaque surfaces at elevated temperatures. *Sol. Energy Mater. Sol. Cells* **132**, 640–649 (2015).
 41. Cao, F. *et al.* Enhanced Thermal Stability of W-Ni-Al 2O_3 Cermet-Based Spectrally Selective Solar Absorbers with Tungsten Infrared Reflectors. *Adv. Energy Mater.* **5**, 1401042 (2015).
 42. Brandt, R., Bird, C. & Neuer, G. Emissivity reference paints for high temperature applications. *Measurement* **41**, 731–736 (2008).
 43. Coblenz, W. W. Harnessing heat from the sun. *Sci. Am.* **127**, 324 (1922).
 44. Durst, T., Harris, L. B. & Goldsmid, H. J. Studies of a thermoelectric generator from tubular solar collectors. *Sol. Energy* **31**, 421–425 (1983).
 45. NREL. Concentrating Solar Power Research. (2012).
 46. Domenicali, C. A. Irreversible Thermodynamics of Thermoelectric Effects in Inhomogeneous, Anisotropic Media. *Phys. Rev.* **92**, 877–881 (1953).
 47. Liu, W. *et al.* Understanding of the contact of nanostructured thermoelectric n-type $\text{Bi}_2\text{Te}_{2.7}\text{Se}_{0.3}$ legs for power generation applications. *J. Mater. Chem. A* **1**, 13093–13100 (2013).

Acknowledgments: This material is partially based upon work supported as part of the Sunshot Initiative funded by the U.S. Department of Energy, Office of Energy Efficiency & Renewable Energy under Award Number: DE-EE0005806 (for device engineering) and based upon work supported as part of the Solid State Solar-Thermal Energy Conversion Center (S³TEC), an Energy Frontier Research Center funded by the U.S. Department of Energy, Office of Science, Office of Basic Energy Sciences under Award Number: DE-SC0001299/DE-FG02-09ER46577 (for materials)

Authors contributions: D.K. carried out modeling and simulation, CSTEg fabrication and experiments, and prepared the manuscript; Q.J. and W.S.L. fabricated the thermoelectric and contact materials; K. M. contributed to CSTEg fabrication and experiments and device modeling; F.C. fabricated spectrally-selective solar absorbers; L.W. contributed to manuscript preparation and CSTEg fabrication and experiments; J.L. contributed to CSTEg fabrication and experiments; Z.F.R. directed research at UH; G.C. directed research at MIT and contributed to the manuscript preparation.

Supporting Online Material for

~~High performance~~ eConcentrating solar thermoelectric generators with a peak efficiency of 7.4%

Daniel Kraemer, Qing Jie, Kenneth McEnaney, Feng Cao, Weishu Liu, Lee A. Weinstein,
James Loomis, Zhifeng Ren,^{*} and Gang Chen^{*}

^{*}Corresponding authors: gchen2@mit.edu, zren@uh.edu

This supplement contains

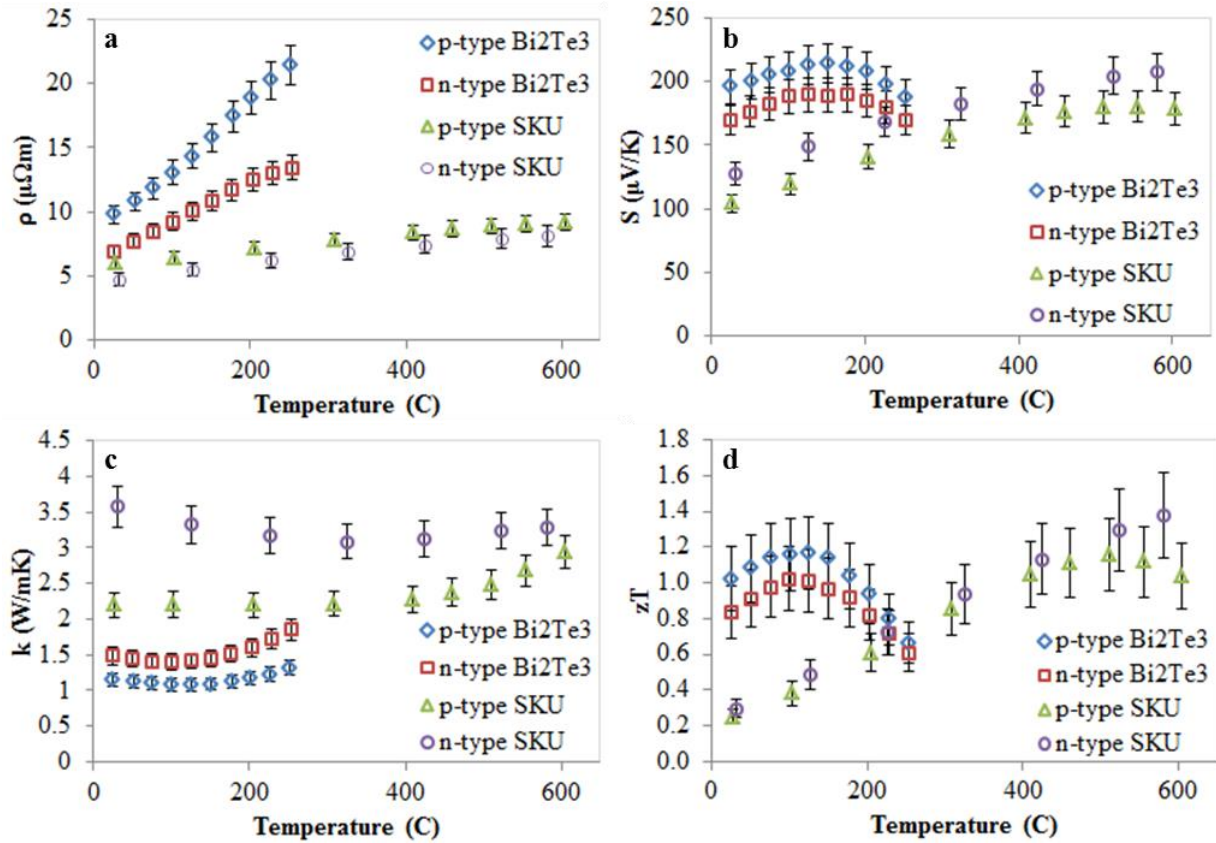
Supplementary Figures ~~S1-S~~10

Supplementary Tables ~~S~~1 and ~~S~~2

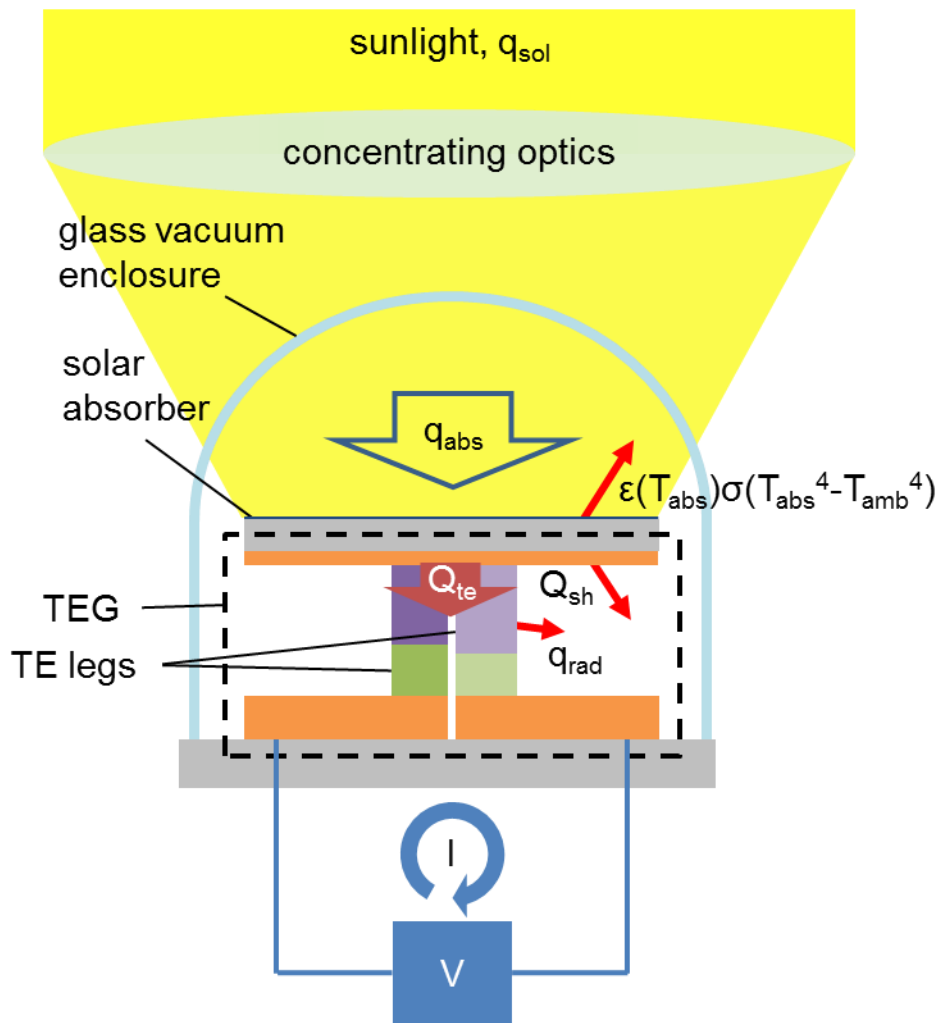
Supplementary ~~Modeling Methods~~ 1-3

~~Experimental details: materials, device fabrication and device testing~~

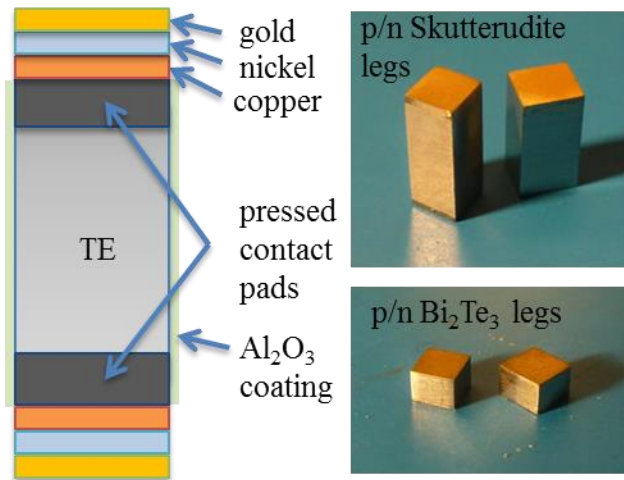
Supplementary References



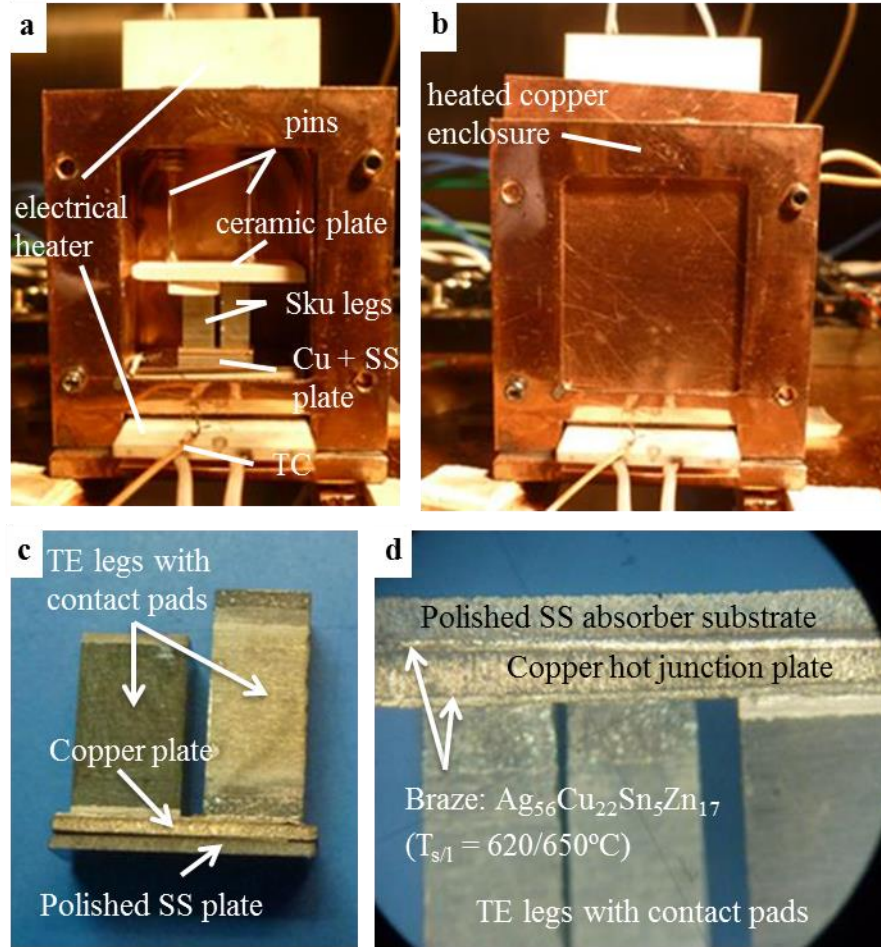
Supplementary Figure S1 | Typical material properties of hot-pressed thermoelectric legs measured with commercial equipment (ZEM 3 and Laser Flash method): p-type Bi_{0.4}Sb_{1.6}Te₃-Sb_{0.01}, n-type Bi₂Te_{2.7}Se_{0.3}+S_{0.015}, p-type Ce_{0.45}Nd_{0.45}Fe_{3.5}Co_{0.5}Sb₁₂, n-type Ba_{0.08}La_{0.05}Yb_{0.04}Co₄Sb₁₂.



Supplementary Figure S2 | CSTEG schematic illustrating heat flows.



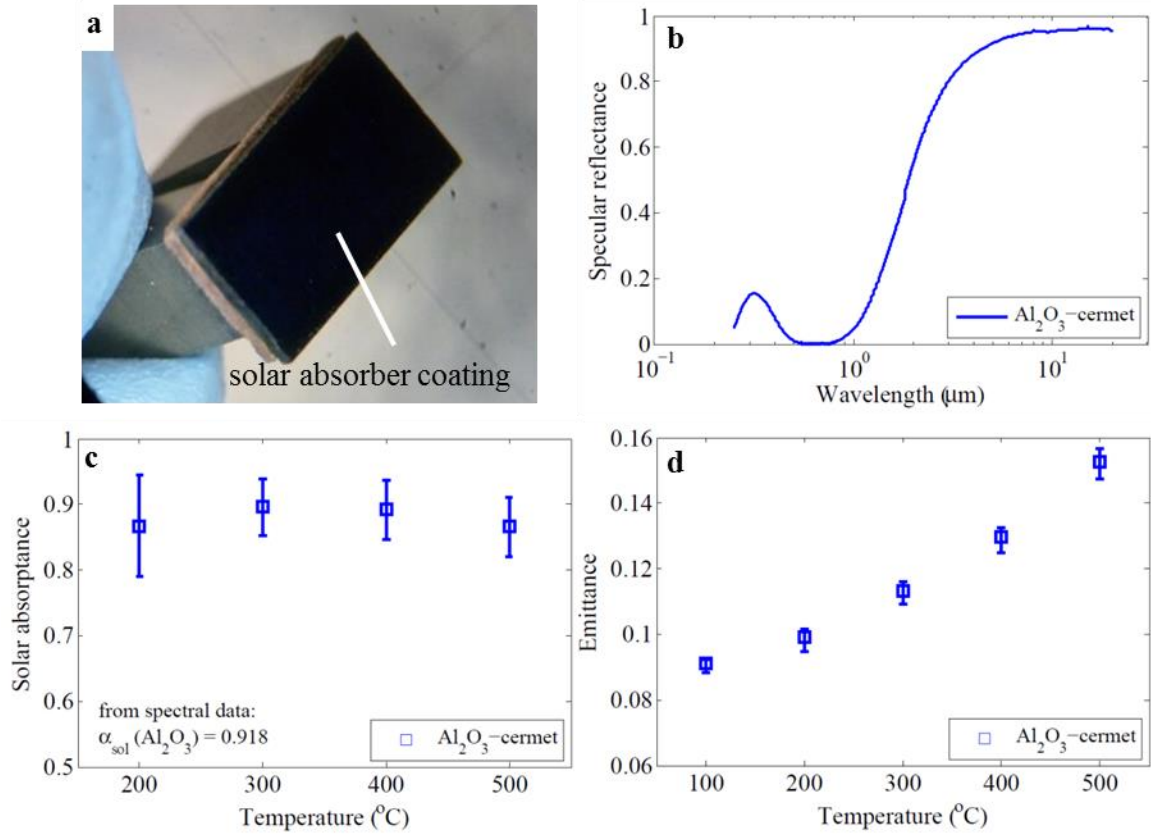
Supplementary Figure S3 | Illustration of layers in individual thermoelectric (TE) legs, which are hot-pressed together with the optimal contact pad material, and photographs of individual legs. To minimize elemental sublimation in vacuum at high temperatures the skutterudite legs are coated with 1 μm Al₂O₃. For more reliable brazing and soldering processes the contact ends are electroplated with copper, nickel and gold.



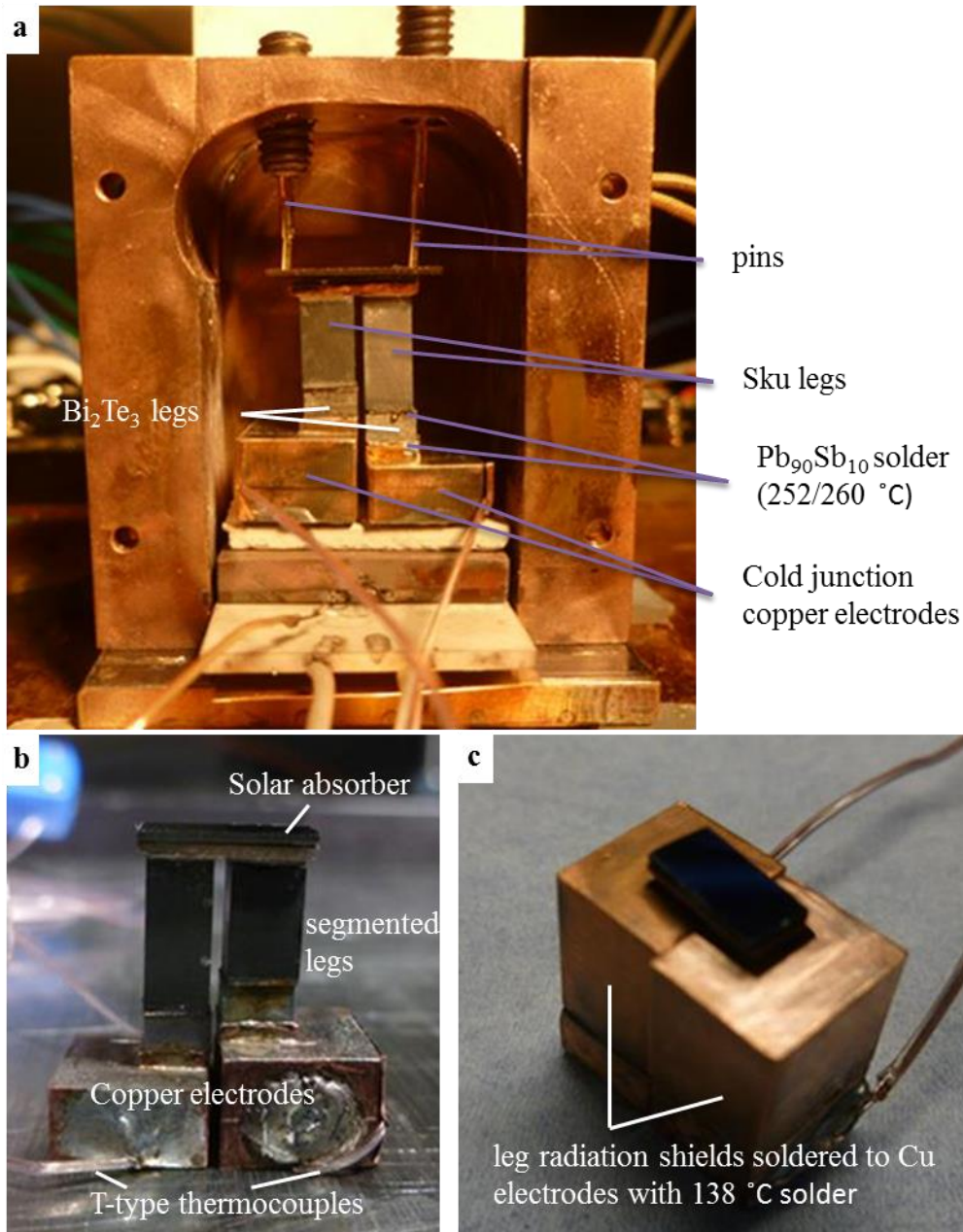
Supplementary Figure S4 | Vacuum brazing process for hot-junction brazed joints and for brazing the stainless steel (SS) absorber substrate to the hot-junction copper plate. (a) Braze assembly: Braze copper enclosure (also shown in (b)) is heated with an electrical heater. Thin-film braze

($\text{Ag}_{56}\text{Cu}_{22}\text{Sn}_5\text{Zn}_{17}$, $T_{s/l} = 618/650^\circ\text{C}$) is sandwiched between the skutterudite (SKU) legs and the copper (Cu) hot-junction plate and the Cu plate and the SS absorber substrate. The pieces are held in place and pushed onto an electrical ceramic heater by 2 spring-loaded pins.

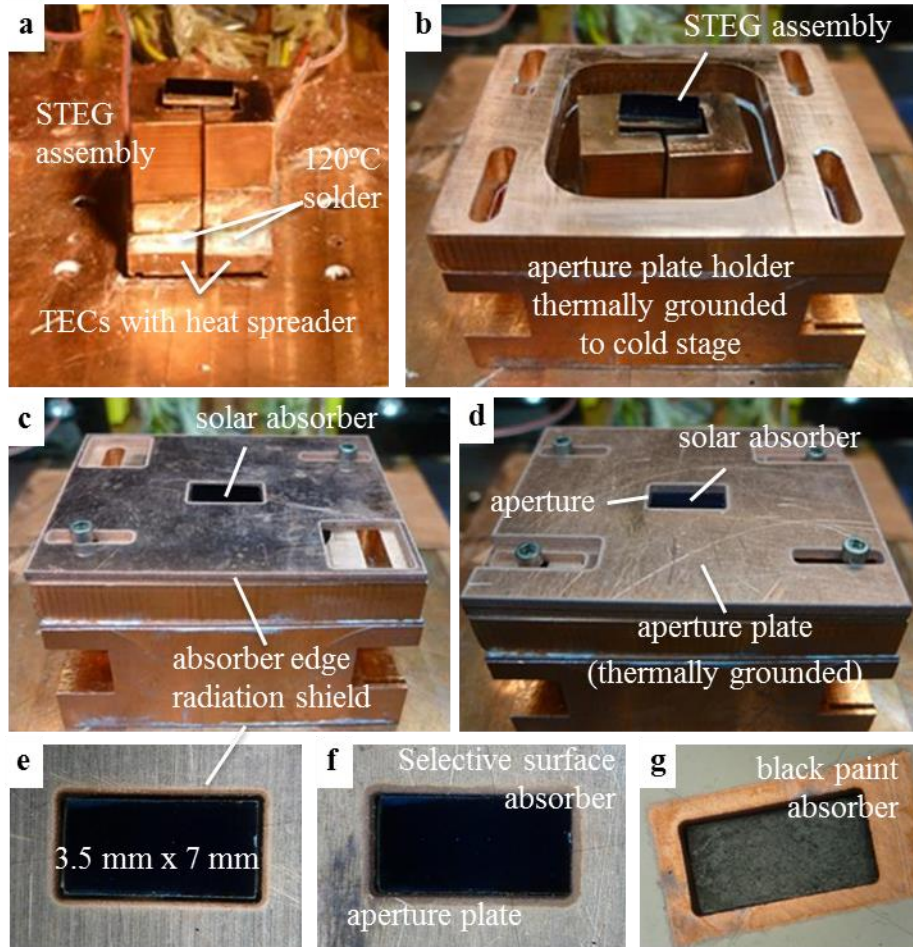
Temperatures of heated braze copper enclosure and the bottom ceramic heater are measured with thermocouples (TC). (c) and (d) Finished SS-Cu-SKU brazed joints.



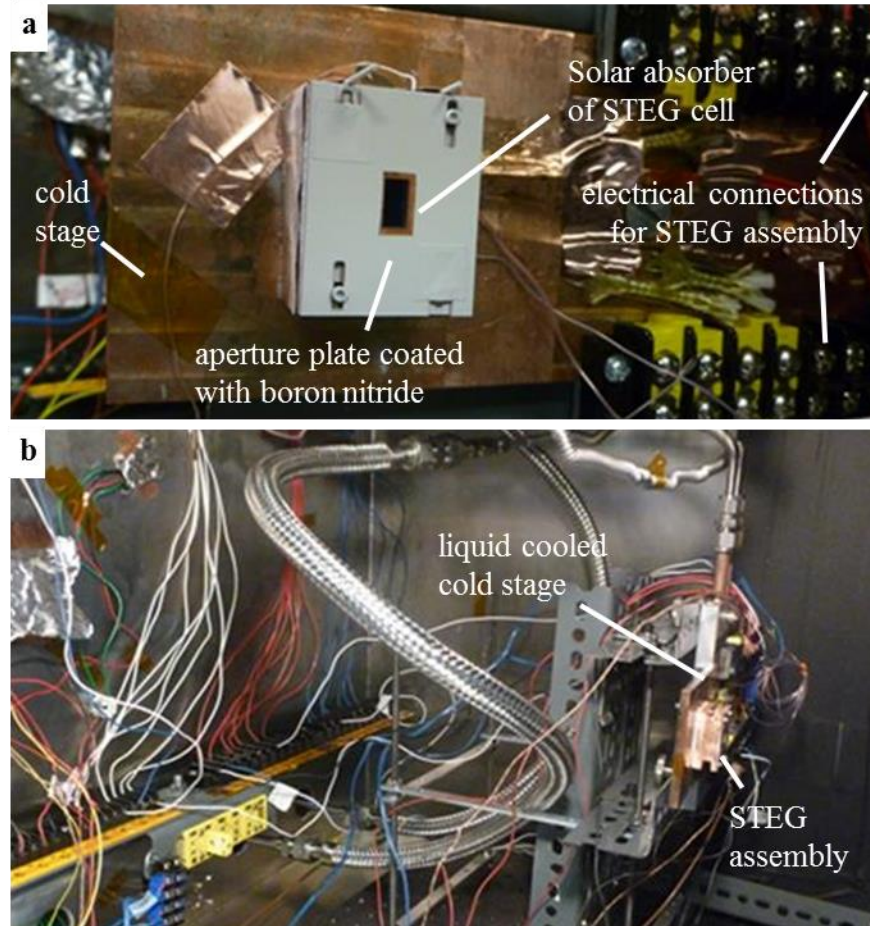
Supplementary Figure S5 | High-temperature spectrally-selective solar absorber of STEG assembly. (a) $\text{Al}_2\text{O}_3\text{cermet}$ -based coating is deposited onto the polished stainless steel absorber substrate after the hot-junction brazing step. (b) – (c) Material properties of solar absorber coating.



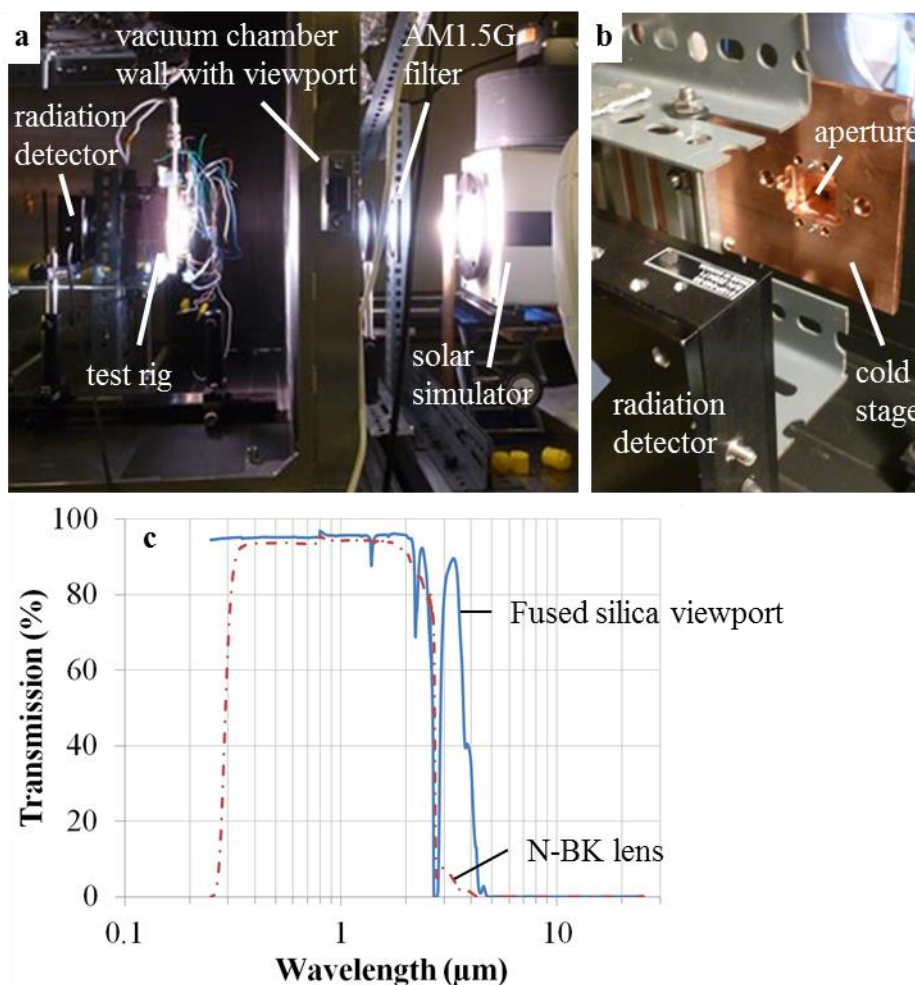
Supplementary Figure S6 | Vacuum soldering process for final STEG fabrication steps. (a) Vacuum soldering setup is the same as the vacuum brazing setup (figure S4(a)). Thin-film solder ($\text{Pb}_{90}\text{Sb}_{10}$, 252/260 °C) is sandwiched between the skutterudite and Bi_2Te_3 legs and between the Bi_2Te_3 and the cold-junction copper electrodes. STEG assembly is held in place and pressed onto a ceramic heater with 2 spring-loaded pins. (b) Fabricated STEG assembly. (c) Fabricated STEG assembly with TE leg radiation shield soldered to the copper electrodes with 138 °C solder.



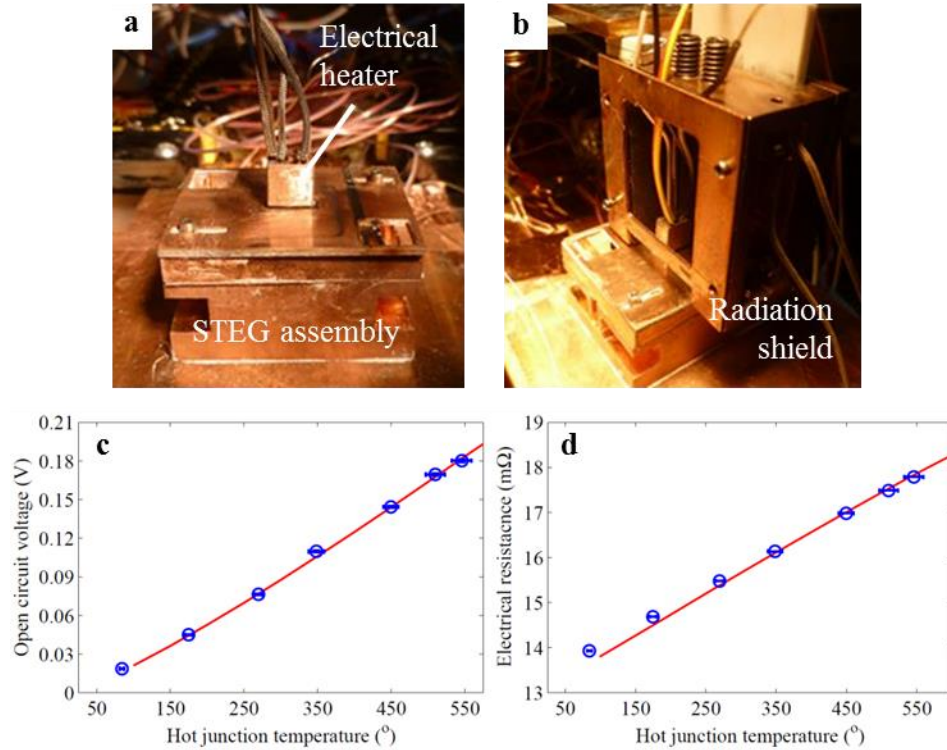
Supplementary Figure S7 | STEG test setup. (a) STEG is soldered (120 °C solder) with its cold-junction copper electrodes onto 2 thermoelectric cooler (TEC) modules enabling accurate cold-junction temperature control. The TECs are soldered onto a liquid-cooled copper cold stage. (b) The STEG is surrounded by the aperture plate holder which is thermally grounded to the cold stage. (c) A solar absorber edge radiation shield closely surrounding the solar absorber (e) is bolted to the aperture holder. (d) The aperture plate is bolted on top of the edge radiation shield plate. (f) The aperture is aligned with the solar absorber of same dimensions. (g) The STEG is also tested with a black paint solar absorber by coating the selective surface with a reference black paint (HE6).



Supplementary Figure S8 | STEG test rig for horizontal solar simulator beam path. (a) STEG assembly is mounted onto the liquid-cooled copper cold stage. The aperture copper plate is spray-coated with boron nitride. (b) The liquid-cooled cold stage with the STEG test setup is mounted vertically inside a vacuum chamber.



Supplementary Figure S9 | Incident power measurement. (a) The radiation coming from the solar simulator transmits through an AM1.5G filter, the fused silica viewport of the vacuum chamber and strikes the test rig. (b) In order to measure the solar radiation passing through the aperture of the STEG assembly, the STEG is removed allowing the solar radiation passing through the aperture to strike a thermopile radiation detector. (c) Measured spectral transmission of the used fused silica viewport and N-BK lens. This spectral data is used to calculate the optical losses and optical efficiency of the experiment.



Supplementary Figure S10 TEG characterization. (a) An electrical heater embedded in a copper enclosure is brazed to the STEG's solar absorber and surrounded by a heated radiation shield (b) to reduce the required electrical power input. (c) The experimentally measured open circuit voltage (markers) as a function of hot-junction temperature of the TEG is in good agreement with calculation results (line) by adding a thermal contact resistance of 5 %. (d) The electrical resistance calculations can be matched with the experiments by introducing a temperature-independent total electrical contact resistance of 2.3 $m\Omega$.

Supplementary Table S1 | Details about used thermoelectric legs.

thermoelectric leg	thermoelectric material	contact pad material + thickness	hot-press temperature	dimensions WxDxL (mm ³)
p-type Skutterudite	Ce _{0.45} Nd _{0.45} Fe _{3.5} Co _{0.5} Sb ₁₂	Fe-based alloy ~0.29 mm	700 °C	3.03x3.00x5.91
n-type Skutterudite	Ba _{0.08} La _{0.05} Yb _{0.04} Co ₄ Sb ₁₂	CoSi ₂ ~0.57 mm	800 °C	2.73x2.73x6.27
p-type Bi ₂ Te ₃	Bi _{0.4} Sb _{1.6} Te ₃ -Sb _{0.01}	Ni ~0.36 mm	500 °C	2.95x2.93x1.75
n-type Bi ₂ Te ₃	Bi ₂ Te _{2.7} Se _{0.3} +S _{0.015}	NiInFeS ~0.32 mm	525 °C	2.61x2.68x1.47

Supplementary Table S2| Thermoelectric bulk material cost analysis.

		p-type				n-type			
material	cost \$/kg	composition	relative cost \$/kg	composition	cost \$/kg	composition	cost \$/kg	composition	cost \$/kg
Bi	15.4	0.4	1.946916553			2	8.182282		
Te	96.3	3	55.75195702			2.7	42.17545		
Sb	8.9	1.6	2.622264703	12	7.26112			12	7.552957
Se	42.2					0.3	1.270749		
S	0.095					0.015	5.81E-05		
Ce	5.5			0.45	0.193638				
Nd	31.8			0.45	0.742354				
Fe	0.065			3.5	0.007094				
Co	30.9			0.5	0.508411			4	4.230758
Ba	550							0.08	3.509536
La	5.72							0.05	0.023074
Yb	3200							0.04	12.86568
TE bulk material cost:			26.0 \$/kg						
TE material weight:			0.89400 gr						
TEG peak power output:			0.5 W						
TE material cost per power output:			0.04643287 \$/W						
references for cost of materials									
Bi	https://www.metalprices.com/p/Metal_Index								
Te	https://www.metalprices.com/p/Metal_Index								
Sb	https://www.metalprices.com/p/Metal_Index								
Se	https://www.metalprices.com/p/Metal_Index								
S	http://minerals.usgs.gov/minerals/pubs/commodity/sulfur/mcs-2015-sulfu.pdf								
Ce	https://www.metalprices.com/p/Metal_Index								
Nd	https://www.metalprices.com/p/Metal_Index								
Fe	https://www.metalprices.com/p/Metal_Index								
Co	https://www.metalprices.com/p/Metal_Index								
Ba	http://www.chemicool.com/elements/barium.html								
La	https://www.metalprices.com/p/Metal_Index								
Yb	http://www.baotou-rareearth.com/yb.html#metal								

Supplementary Methods

S1-Supplementary Method 1 | -Modeling

Our modeling approach has been described in detail in multiple previous publications.^{1,2,3,4} We only give a short summary here.

S1.1 Thermoelectric couple modeling

First, the performance characteristics (efficiency, hot-junction heat input, electrical power output, etc.) of the individual segmented thermoelectric legs are calculated using the temperature-dependent properties of the thermoelectric materials ([supplementary figure S1](#)) and Domenicali's coupled 1st order equations which are modified to include the effect of leg radiation heat loss.^{4,5}

$$\frac{dT}{dx} = \frac{i(ST)_x - q_{leg}(x)}{k(x)} \quad (S1)$$

$$\frac{dq_{leg}}{dx} = \left[i\rho(x) + S(x) \frac{i(ST)_x - q_{leg}(x)}{k(x)} \right] i - \frac{Pq_{rad}(x)}{A_{leg}} \quad (S2)$$

Those coupled first-order equations are solved iteratively for the n- and p-type elements for the optimal thermoelectric heat flux and temperature distribution corresponding to the optimum current densities for a specified TEG geometry (lengths and cross-sectional areas of thermoelectric elements). Equation (S1) correlates the local temperature gradient $dT(x)/dx$ to the local heat flow density, $q_{leg}(x)$, the current density $i = I/A_{leg}$ with I and A_{leg} being the applied current and the cross-sectional area of the thermoelectric leg, respectively, the local thermal conductivity, $k(x)$, and Seebeck coefficient, $S(x)$ due to their dependence on local temperature $T(x)$. Equation (S2) correlates the local change in the heat flow density, $dq_{leg}(x)/dx$ with the local electrical resistivity $\rho(x)$. The last term on the right hand side of equation (S2) appears due to the radiative heat transfer between the thermoelectric leg and the surroundings with P being the leg perimeter. In the case of a TEG with two closely-spaced thermoelectric legs we assume negligible radiation heat loss from the side walls facing each other. Thus, only 3 side-walls of the thermoelectric leg contribute to the radiative heat transfer with the surroundings. The local leg radiation power density can be defined as $q_{rad} = \epsilon_{eff}(T(x))\sigma(T(x)^4 - T_c^4)$ with ϵ_{eff} being the effective leg IR emittance, σ the Stefan-Boltzmann constant and T_c being the surrounding cold-side temperature. For $dx \rightarrow 0$ the equations (S3) and (S4)(S2) can be written for the i^{th} segment as:

$$T_{j+1} = T_j + \frac{dx}{k_j} [iT_j S_j - q_{leg,j}], \quad (j = 0, 1, 2, \dots, n-1) \quad (S3)$$

$$q_{j+1} = q_j + \left[q_j i^2 \left(1 + \frac{S_j^2 T_j}{\rho_j k_j} \right) - \frac{i S_j q_j}{k_j} - \frac{3 q_{rad,j}}{A_{leg}} \right] dx, \quad (j = 0, 1, 2, \dots, n-1) \quad (S4)$$

The output from one segment of the leg becomes the input for the adjacent segment, such that the iterative method⁶ can be used to accurately determine the temperature and heat flow profile of the thermoelectric leg for each applied electrical current with T_{CJ} and T_{HJ} as the specified cold and hot junction temperature boundary conditions. From that the heat flow at the hot junction, $Q_{leg,HJ} = q_{leg,n} \cdot A_{leg}$, the created thermoelectric leg voltage, $V_{leg} = \sum_0^{n-1} S_j (T_{j+1} - T_j) + i \sum_0^{n-1} \rho_j dx$, the thermoelectric leg power output, $P_{leg} = V_{leg} I$, and leg conversion efficiency, $\eta_{leg} = \frac{P_{leg}}{Q_{leg}}$ at every given electrical current is determined. It shall be noted that for the defined x direction the current and heat flow densities are negative for a p-type thermoelectric leg.

The optimization is performed for both thermoelectric legs with the same length. Due to the difference in the n - and p -type thermoelectric material properties, the cross-sectional area of the thermoelectric elements are different and the cross-sectional area ratio must be optimized using the iteration process. The boundary conditions for the differential equations of both thermoelectric elements are the same fixed cold- and hot-junction temperatures that uniquely determine the optimal current, the temperature and heat flux distribution for the specified single-couple TEG geometry. The thermoelectric efficiency can be calculated with $\eta_{te} = \frac{P_{te}}{Q_{te}} =$

$\frac{I(V_{leg,p} + V_{leg,n})}{Q_{leg,p} + Q_{leg,n}}$. Electrical contact resistances can easily be included in the calculations by adding segments with corresponding electrical resistivity and a negligible Seebeck coefficient to the hot and cold end of the thermoelectric elements.

S1.2 CSTEg modeling

The CSTEg test devices consist of one thermoelectric couple sandwiched between the solar absorber and a heat sink ([supplementary figure S2](#)). Knowing the heat flow into the thermoelectric couple, Q_{te} , the energy balance for the solar absorber with negligible temperature gradients yields

$$Q_{teg} = Q_{te} + Q_{sh} = \alpha_{sol} A_{abs} q_{abs} - A_{abs} \varepsilon(T_{abs}) \sigma (T_{abs}^4 - T_{amb}^4) \quad (S5)$$

with Q_{teg} being the hot-side heat input power to the TEG determined by the heat flow into the thermoelectric couple and possible thermal radiation shunting heat loss, Q_{sh} , from the edges and the back side of the solar absorber to the surroundings. The heat flow, Q_{teg} , at a given CSTEg operating temperature difference must be balanced in steady state by the absorbed solar radiation (first term on the right hand side of S5) and the radiation heat loss from the solar absorber surface (second term on the right hand side). The absorbed solar radiation is dependent on the solar absorptance, α_{sol} , the absorber area, A_{abs} , and the incident absorber solar radiation flux density, $q_{abs} = \eta_{opt} C_{opt} q_{sol}$ determined by the optical efficiency, the optical solar concentration and the solar intensity striking the concentrating optics. The infrared radiation heat loss from the solar absorber surface is determined by its total-hemispherical emittance, $\varepsilon(T_{abs})$, and operating temperature, T_{abs} , and surrounding temperature, T_{amb} . The assumption of a uniform solar absorber/hot-junction temperature only holds under certain design restrictions which are

discussed in great detail in one of our previous publications.⁴ One of our design solutions to address the challenge of efficient thermal concentration is to use a thick hot-junction copper plate with the same area as the stainless steel substrate of the solar absorber. This allows the absorbed solar radiation to be conducted to the thermoelectric legs with negligible temperature gradients. From the correlation (S5) the absorber efficiency can be obtained as

$$\eta_{abs} = \frac{Q_{teg}}{A_{abs}q_{abs}} = \alpha_{sol} - \frac{\varepsilon(T_{abs})\sigma(T_{abs}^4 - T_{amb}^4)}{\eta_{opt}C_{opt}q_{sol}} \quad (S6)$$

The TEG efficiency includes the possible thermal shunting losses, Q_{sh} , and can be expressed as

$$\eta_{teg} = \frac{I(V_{leg,p} + V_{leg,n})}{Q_{te} + Q_{sh}} = \frac{P_{te}}{Q_{teg}} \quad (S7)$$

Therefore, the CSTEG efficiency can be calculated with a given optical efficiency, η_{opt} , for the concentrating optics with

$$\eta = \frac{q_{abs}}{C_{opt}q_{sol}} \frac{(q_{te} + (C_{th} - 1)q_b + A_e/A_{te}q_e)}{C_{th}q_{abs}} \frac{P_{te}}{Q_{teg}} = \eta_{opt}\eta_{abs}\eta_{teg} \quad (S8)$$

where C_{opt} is the optical concentration (area ratio), q_{sol} the solar intensity, q_{abs} the solar flux density incident on the solar absorber, q_{te} the hot-junction heat flux density of the thermoelectric couple, q_b and q_e the thermal radiative heat flux densities of the back side and edges of the solar absorber, respectively, with A_e being the edge area and $C_{th} = A_{abs}/A_{te}$ being the thermal concentration ratio defined as the ratio of the solar absorber area to the cross-sectional area of the thermoelectric couple.

To simulate the experimental results, the temperature-dependent properties of the p-type and n-type elements as shown in [supplementary figure S1](#) and their typical dimensions as shown in [supplementary table S1](#) were used. We modify the Seebeck coefficient and electrical resistance of the thermoelectric couple according to measured results from the TEG characterization experiment which is discussed later. For the optical properties of the solar absorber we use the typical measured solar absorptance and temperature-dependent total hemispherical emittance of the selective absorbers as shown in [supplementary figure S5](#). The emittance values and their temperature dependence of the thermoelectric legs and the back side and edges of the solar absorber are less accurately known. Hence, these emittance values are treated as fitting parameters. Values obtained, however, are within reason.

Supplementary Method 2 |S2: Fabrication of STEG Assembly

The fabrication of a STEG cell for proof of concept testing is not a straightforward task and the process required careful optimization. In addition to the fabrication and optimization of the individual thermoelectric elements (including contact pad materials) the main challenge of the

STEG cell fabrication is joining 4 individual thermoelectric legs to a mechanically strong segmented-leg single-couple TEG with reasonably low contact resistances without negatively affecting their material properties. Furthermore, a high-temperature solar absorber needs to be attached to the hot junction of the single-couple TEG with minimal thermal resistance and without damaging the absorber surface. The optimized fabrication process is described in the following sections.

S2.1 Preparation of thermoelectric legs

The thermoelectric material is ball-milled and hot-pressed together with the contact pad material to a sample disc equivalent to the process described in previous publications.⁷ The hot-press temperatures are given in [supplementary](#) table S1. Each thermoelectric disc is hot-pressed to the optimal thickness obtained by the single segmented TE leg solver (modeling section) that optimizes the leg lengths of the Bi_2Te_3 and the skutterudite leg section for maximum segmented TE leg efficiency while maintaining the total length of the segmented leg constant. The thermoelectric discs are then cut to individual TE legs with optimal cross-sectional areas leading to maximum single-couple TEG efficiency. The geometry optimization of the segmented TE legs is performed with typical material properties of the fabricated TE materials as shown in [supplementary](#) figure S1.

For a successful lab-scale device test the cross-sectional area of the TE legs should be large while the length of the segmented TE legs should be minimized in order to minimize the effect of leg radiation as long as the electrical contact resistances are negligible. However, there are two experimental limitations that put constraints on the TE leg dimensions. (1) The minimum TE disc thickness is approximately 1.5 mm for the used hot-press process. This sets the minimum segmented TE leg length. (2) The maximum cross-sectional areas of the TE legs are determined by the maximum solar radiation power and/or maximum electrical current that can be supplied to the CSTEG by the solar simulator and power supply, respectively. Details about the fabricated TE legs including typical dimensions used in the experiments are shown in table S1.

Further preparation of the TE legs is required before they can be assembled into a segmented-leg single-couple TEG. The final TE legs are shown in [supplementary](#) figure S3. The skutterudite legs are coated with a 1 μm thick Al_2O_3 film to minimize sublimation of elements with high vapor pressures such as antimony during the high-temperature vacuum brazing process. The end surfaces of the contact pads are polished, cleaned and electroplated with copper, nickel and gold for more reliable brazing and soldering processes.

S2.2 High-temperature vacuum brazing process

A high-temperature vacuum brazing process ([supplementary figure S4](#)) is developed to join the p- and n-type skutterudite legs with a copper hot-junction plate using a silver-based thin foil braze ($\text{Ag}_{56}\text{Cu}_{22}\text{Sn}_5\text{Zn}_{17}$, solidus/liquidus = 618/650 °C). Additionally, the stainless steel solar absorber substrate is simultaneously brazed to the hot-junction copper plate with the same type of thin foil braze to ensure excellent mechanical and thermal contact between the solar absorber and the hot-junction of the single-couple TEG. It is important that the spectrally-selective surface of the solar absorber is deposited on the stainless steel substrate after the high-temperature brazing step to avoid affecting its optical properties. There are several reasons for performing the brazing process in a vacuum. (1) No oxidation of surfaces during the high-temperature brazing. (2) If the contact surfaces are not oxidized and are clean, there is no braze flux required as the latter can damage and/or contaminate the thermoelectric material and is difficult to remove without leaving residue on the CSTEg's surfaces. Thus, (3) it is a clean brazing process which leads to minimal increase in IR emittance of the CSTEg's surfaces. (4) It is a controlled brazing process in terms of brazing temperature, time and environment which is especially important because the brazing temperatures are close to the skutterudite hot-pressing temperatures (table S1).

[Supplementary Figures S4\(a\)](#) and [\(b\)](#) show the brazing setup. It consists of a copper enclosure heated by a ceramic heater and a second bottom heater which can quickly change temperature by adjusting its electrical power input. The skutterudite legs, the hot-junction copper plate and the stainless steel solar absorber substrate with thin-film braze in between the interface are held in place and pressed onto the bottom ceramic heater with 2 spring-loaded pins. The temperatures of the copper enclosure and the bottom ceramic heater are measured with thermocouples. Long term high-temperature exposure (>550 °C) of the skutterudite legs can affect their material properties and/or their interfaces with the contact pads. High temperatures close to the hot-press temperatures can promote accelerated sublimation of high vapor pressure elements, elemental diffusion between thermoelectric and contact pad materials and undesired annealing processes. For a good brazing joint, however, the brazing parts must be heated uniformly to above the liquidus point of the braze of 650 °C. In order to minimize the time when the skutterudite legs are at temperatures above 550 °C, the copper enclosure is heated to 680 °C as quickly as possible. The bottom heater is thermally grounded to the liquid cooled cold stage which stays near room temperature. This causes the bottom heater and the skutterudite legs to lag behind in temperature by approximately 110 °C. As soon as the copper enclosure reaches 660 °C while the skutterudite legs only reach ~550 °C, the bottom heater is turned on to rapidly heat the brazing parts to above 680 °C. When the copper enclosure reaches 680 °C both ceramic heaters are turned off and the vacuum chamber is purged with argon gas for rapid cooling of the skutterudite legs to below 550 °C. This process limits the high-temperature exposure of the skutterudite legs to less than 3 minutes and ensures the temperature does not significantly exceed 680 °C. Some successfully brazed skutterudite copper hot-junction examples with brazed stainless steel solar absorber substrates are shown in [supplementary figures S4\(c\)](#) and [\(d\)](#). The hot-junction copper plate is chosen to be the same size as the stainless steel solar absorber substrate (3.5 mm x 7 mm) to minimize temperature gradients in the solar absorber.

S2.3. Deposition of spectrally-selective solar absorber surface

In order to prevent damaging the spectrally-selective solar absorber coating by high-temperature exposure (higher than 600 °C), deposits of evaporates and/or scratches from the brazing process, the spectrally-selective solar absorber surface stack is sputtered onto the polished stainless steel substrate after the high-temperature vacuum brazing process. The selective surface stack used for the fabricated CSTEg cell is based on a W-Ni-Al₂O₃-cermet double layer with 2 anti-reflection coatings and the tungsten IR-reflector layer which improves the spectral selectivity and also acts as an elemental diffusion barrier providing high-temperature stability up to 600 °C in vacuum ([supplementary figure S5](#)).⁸ The expected optical properties of the solar absorber are shown in [supplementary figures S5\(b\)-\(d\)](#) with a temperature-independent solar absorptance of ~0.91 and a monotonically increasing total hemispherical emittance of ~0.09 at 100 °C to ~0.15 at 500 °C suggesting approximately 0.18 at 600 °C.

S2.4. Low-temperature vacuum soldering process

The last task of the single-couple TEG fabrication is to solder the Bi₂Te₃ low-temperature legs to the cold ends of the skutterudite legs and the cold junction copper electrodes to the cold ends of the Bi₂Te₃ legs. The two joints are soldered simultaneously using thin film Pb₉₀Sb₁₀ solder (solidus/liquidus = 250/260 °C) and a vacuum soldering process similar to the vacuum brazing process described earlier with the only difference being the lower temperatures ([supplementary figure S6\(a\)](#)). The skutterudite hot-junction assembly with aligned Bi₂Te₃ legs and cold-junction copper electrodes is held in place and pushed onto the bottom ceramic heater. The skutterudite-Bi₂Te₃ and Bi₂Te₃-electrode interfaces are filled with thin-film solder. Under vacuum the system is rapidly heated to approximately 270 °C using the 2 ceramic heaters.

[Supplementary Figure S6\(b\)](#) shows the fabricated couple CSTEg assembly based on skutterudite-Bi₂Te₃ segmented legs. T-type thermocouples are soldered to the cold-junction copper electrodes with Pb₆₃Sn₃₇ solder (183 °C). The copper wires of the T-type thermocouples are also used to measure the voltage of the CSTEg during the experiments. In order to minimize radiation heat losses from the TE legs, copper radiation shields are placed around them as shown in [supplementary figure S6\(c\)](#).

Supplementary Method 3 |S3. Experimental Testing Method

S3.1. CSTEg test setup

The CSTEg test setup for the proof-of-concept experiment is shown in [supplementary figures figs. S7 and S8](#). The fabricated STEg is soldered with its cold-junction copper electrodes to two individually controlled thermoelectric cooler modules (TECs) to enable quick and accurate cold-junction temperature control ([supplementary figure S7\(a\)](#)). The TECs are soldered onto a liquid-cooled cold stage which is maintained at a constant temperature to remove the excess heat from the TECs and minimize temperature drifts of the system. In practical systems, we expect the

cold side would have a passive heat spreader and use natural convection cooling, as mentioned in the manuscript.

The solar absorber is tightly surrounded by an edge radiation shield ([supplementary figures-figs. S7\(c\) and \(e\)](#)) to minimize radiation heat losses. An aperture of same dimensions as the solar absorber is placed in front of it ([supplementary figures-figs. S7\(d\) and \(f\)](#)) for accurate determination of the incident solar radiation power as discussed in more detail in [the following section \(“Incident solar radiation power measurement”\)](#)[S3.2](#); only light passing through that aperture strikes the solar absorber while all other light is reflected away by the aperture plate. If the radiation shield and aperture plate temperature would rise significantly above room temperature due to absorbed solar radiation, the heat losses from the solar absorber would unrealistically be reduced and affect experimental STEG performance results. Therefore, the edge radiation shield and the aperture copper plate are thermally grounded to the cold stage via the copper holder surrounding the STEG assembly ([supplementary figure S7\(b\)](#)) to minimize the temperature rise. The liquid-cooled cold-stage temperature can be adjusted to close to -20°C which helps to maintain the aperture plate temperature to below 35°C during all experiments. As shown in [supplementary figure S8\(a\)](#) the copper aperture plate is coated with white boron nitride spray to increase diffuse reflection and IR emittance to reduce multiple reflection effects within the vacuum chamber for accurate incident solar power measurement, and to further limit the temperature rise.

In addition to experiments with a STEG based on a spectrally-selective solar absorber, a STEG based on a solar absorber with black reference paint (HE6) is tested ([supplementary figure S7\(g\)](#)). While the spectrally-selective surface has a solar absorptance of ~ 0.91 and a low IR emittance of $0.15 - 0.18$ in the temperature range of $500 - 600^{\circ}\text{C}$, the black reference paint is a gray surface with a temperature-independent absorptance and emittance of 0.95 .^{9,10}

S3.2.-Incident solar radiation power measurement

[Supplementary Figures S8\(b\) and figure S9](#) show the CSTEg test rig mounted inside the vacuum chamber for a horizontal solar simulator beam path. One of the most challenging quantities to measure accurately is the incident solar radiation power. We tested the thermopile used for incident solar power measurement in terms of illumination spot size and no variation in the detected power level was observed at our radiation power density levels. As mentioned the aperture in front of the solar absorber of the CSTEg determines the solar radiation power input to the CSTEg. In order to measure the solar radiation power passing through the aperture, the aperture plate is mounted onto an identical cold stage without the CSTEg ([supplementary figure S9\(b\)](#)). The cold-stage copper plate has a large opening allowing the solar radiation that passed through the aperture to strike and be measured by a thermopile detector ([supplementary figures S9\(a\) and \(b\)](#)). The used solar simulator supplies a rather non-uniform beam spot. Thus, after the incident power measurement the cold stage with the CSTEg assembly must be mounted such that the aperture is in the same location as for the incident power measurement. Furthermore, to ensure an accurate incident radiation power measurement, it is important that the optics (viewport, possible focusing lens) in the path of the solar simulator beam do not significantly alter the broad wavelength spectrum of the radiation. The used thermopile is calibrated for the radiation spectrum of the used solar simulator. Thus, in case of a changing radiation spectrum the thermopile would need to be calibrated accordingly. Additionally, while the radiation

spectrum is not of significant importance for a gray surface such as the used black reference paint, it can affect the integrated absorptance of a spectrally-selective solar absorber. However, as shown in [supplementary figure S9\(c\)](#) the spectral transmittance of the fused silica viewport and an N-BK lens is close to being constant up to about 2 μm which corresponds to more than 95 % of the solar simulator beam power.

S3.3. CSTEg experiments

The experiments are performed under high vacuum ($<10^{-4}$ mbar) in a large vacuum chamber. This configuration does not favor photons emitted by the device to be reflected back, i.e., photon recycling, and hence tends to reduce the efficiency. The experiment is controlled with LabVIEW which includes the cold-junction temperature control and the STEg current setting and voltage measurement. For accurate power output measurements the STEg must reach steady state for each current set point before recording the current and voltage. The electrical current is supplied with a high current power supply and the STEg voltage is measured with a precision Keithley digital multimeter with nV resolution.

S3.4. TEG characterization

The hot-junction temperature is not measured during the CSTEg experiment to avoid the heat losses from an attached thermocouple. However, an additional TEG characterization is performed after the CSTEg experiment to gain more insight in the CSTEg performance by measuring the open circuit voltage and electrical resistance of the TEG as a function of hot-junction temperature with constant cold-junction temperature at 25 $^{\circ}\text{C}$ ([supplementary figure S10](#)). The solar absorber surface is removed from the stainless steel substrate and a heater assembly with a copper enclosure is brazed to it ([supplementary figure S10\(a\)](#)). The hot-junction temperature is measured with a thermocouple embedded in the copper enclosure of the heater assembly. The hot-junction heater assembly is surrounded by a heated copper radiation shield to reduce the hot-junction heater power input ([supplementary figure S10\(b\)](#)). The experimentally measured open circuit voltage can be matched with simulations by adding a 5 % thermal contact resistance ([supplementary figure S10\(c\)](#)). The experimental electrical resistance trend is matched by adding a constant total electrical contact resistance of 2.3 m Ω ([supplementary figure S10\(d\)](#)). Even though we can accurately simulate the Seebeck voltage and electrical resistance by adding contact resistances it is also possible that the actual Seebeck coefficient and electrical resistivity of the used thermoelectric legs are different. Nevertheless, the contact resistances are included in the CSTEg model to simulate the CSTEg performance.

S3.5. Obtaining absorber and TEG efficiencies

Knowing the performance of the individual sub-systems (solar absorber and TEG) during the CSTEg experiment is helpful to analyze the STEg performance. By characterizing the fabricated TEGs as discussed in S3.4, the solar absorber temperature can be obtained during the CSTEg experiment. The absorber efficiency can be calculated (Eq. S6) if the solar absorptance and total-hemispherical emittance are known for the operating temperatures. With the absorber efficiency and measured STEg efficiency (optical losses excluded, i.e., $\eta_{\text{opt}} = 1$), the TEG

efficiency can be calculated using Eq. S8. Since the commercial reference black paint HE6 has accurately known temperature-independent solar absorptance and total-hemispherical IR emittance of 0.95, we used the STEG efficiency results with black paint absorber to determine the TEG efficiency. This eliminates the need to perform a separate TEG efficiency measurement with an electrical hot-junction heater, which would come with significant challenges of its own. Thus measured TEG efficiency as a function of absorber/hot-junction temperature can also be used to determine (Eq. S8) the absorber efficiency when the spectrally-selective solar absorber is used in the STEG experiment. These results are in reasonable agreement with the calculated absorber efficiency using the optical properties of the spectrally-selective solar absorber ([supplementary Fig. 2f](#)).

References

1. Kraemer, D. *et al.* High-performance flat-panel solar thermoelectric generators with high thermal concentration. *Nat. Mater.* **10**, 532–538 (2011).
2. Kraemer, D., McEnaney, K., Ren, Z. & Chen, G. in *Thermoelectr. its Energy Harvest. Modul. Syst. Appl. Thermoelectr.* (Rowe, D. M.) 1–18 (CRC Press - Taylor & Francis Group, LLC, 2012). doi:10.1201/b11892
3. McEnaney, K., Kraemer, D., Ren, Z. & Chen, G. Modeling of concentrating solar thermoelectric generators. *J. Appl. Phys.* **110**, 074502 (2011).
4. Kraemer, D., McEnaney, K., Chiesa, M. & Chen, G. Modeling and optimization of solar thermoelectric generators for terrestrial applications. *Sol. Energy* **86**, 1338–1350 (2012).
5. Domenicali, C. A. Irreversible Thermodynamics of Thermoelectric Effects in Inhomogeneous, Anisotropic Media. *Phys. Rev.* **92**, 877–881 (1953).
6. Hogan, T. P. in *Thermoelectr. Handb. Macro to Nano* (Rowe, D. M.) (Taylor & Francis Group, LLC, 2006).
7. Kraemer, D. *et al.* High thermoelectric conversion efficiency of MgAgSb-based material with hot-pressed contacts. *Energy Environ. Sci.* **8**, 1299–1308 (2015).
8. Cao, F. *et al.* Enhanced Thermal Stability of W-Ni-Al₂O₃ Cermet-Based Spectrally Selective Solar Absorbers with Tungsten Infrared Reflectors. *Adv. Energy Mater.* **5**, (2015).
9. Brandt, R., Bird, C. & Neuer, G. Emissivity reference paints for high temperature applications. *Measurement* **41**, 731–736 (2008).
10. Kraemer, D., McEnaney, K., Cao, F., Ren, Z. & Chen, G. Accurate determination of the total hemispherical emittance and solar absorptance of opaque surfaces at elevated temperatures. *Sol. Energy Mater. Sol. Cells* **132**, 640–649 (2015).